



Effect of atomic layer deposited zinc promoter on the activity of copper-on-zirconia catalysts in the hydrogenation of carbon dioxide to methanol

Aitor Arandia^{a,*}, Jihong Yim^a, Hassaan Warraich^a, Emilia Leppäkangas^a, René Bes^{b,c}, Aku Lempelto^d, Lars Gell^d, Hua Jiang^e, Kristoffer Meinander^f, Tiia Viinikainen^a, Simo Huotari^b, Karoliina Honkala^d, Riikka L. Puurunen^a

^a Department of Chemical and Metallurgical Engineering, School of Chemical Engineering, Aalto University, Kemistintie 1, P.O. Box 16100, FI-00076 Aalto, Espoo, Finland

^b Department of Physics, University of Helsinki, P.O. Box 64, FI-00014 Helsinki, Finland

^c Helsinki Institute of Physics, P.O. Box 64, FI-00014 Helsinki, Finland

^d Department of Chemistry, Nanoscience Center, University of Jyväskylä, P.O. Box 35, FI-40014 Jyväskylä, Finland

^e Department of Applied Physics, Aalto University, P. O. Box 13500, FI-00076 Aalto, Espoo, Finland

^f Department of Bioproducts and Biosystems, School of Chemical Engineering, Aalto University, P. O. Box 16300, FI-00076 Aalto, Espoo, Finland

ARTICLE INFO

Keywords:

Carbon dioxide
Hydrogenation
Methanol
Atomic layer deposition
Copper
Zinc oxide

ABSTRACT

The development of active catalysts for carbon dioxide (CO₂) hydrogenation to methanol is intimately related to the creation of effective metal-oxide interfaces. In this work, we investigated how the order of addition of copper and zinc on zirconia influences the catalytic properties, the catalytic activity and selectivity toward methanol. Regarding the carbon dioxide conversion and methanol production, the catalysts on which the promoter (zinc) was atomically deposited after copper impregnation (i.e., ZnO/Cu/ZrO₂ and ZnO/Cu/ZnO/ZrO₂) were superior catalysts compared to the reverse copper-after-zinc catalyst (Cu/ZnO/ZrO₂). Temperature-programmed experiments and in situ diffuse reflectance infrared Fourier transform-spectroscopy (DRIFTS) experiments allowed us to elucidate the benefits of the zinc-after-copper pair to store CO₂ as carbonate species and further convert them into formate species, key intermediates in the formation of methanol. This research provides insights into the potential of atomic layer deposition in the development of tailored heterogeneous catalysts for efficient CO₂ valorization to methanol.

1. Introduction

Worldwide, there is a great desire to develop technologies for the efficient capture and conversion of carbon dioxide to fuels and chemicals, such as methanol [1–3]. Methanol is a carrier of carbon and hydrogen [4,5] and, as an energy carrier, it can be used directly as a fuel in direct methanol fuel cells (DMFCs) and internal combustion engines (ICEs) [6,7]. Additionally, methanol can be used in the production of high value-added chemicals (e.g. formaldehyde, methyl tert-butyl ether and acetic acid) and as a feedstock to produce hydrocarbons (such as alkanes, olefins or aromatics) and inherently fuels [6–8].

Traditionally, Cu/ZnO-based catalysts have been employed in the industrial production of methanol from the syngas stream (CO/CO₂/H₂)

generated in the steam reforming of natural gas [9–11]. The mechanism of methanol formation from CO/CO₂ has been under debate for decades [12,13]. Since CO is the predominant carbon-containing molecule in syngas [2,12] and Cu is an outstanding metal for CO₂ reduction to CO (through reverse water-gas shift, CO₂ + H₂ ⇌ CO + H₂O), CO has been considered the primary carbon source in methanol production for decades (CO + 2 H₂ ⇌ CH₃OH) [10,12]. It was in the late 1980 s when the use of ¹⁴C-labeled isotopes provided evidence to suggest CO₂ as the main carbon source in the methanol production (CO₂ + 3 H₂ ⇌ CH₃OH + H₂O) from CO₂/CO/H₂ mixtures [14]. Since then, many studies have been driven in the same direction [10,12,15–17], and currently, CO₂ is perceived as the major reactant under industrial conditions. However, as Grabow and Mavrikakis suggested based on density functional theory

* Corresponding author.

E-mail address: aitor.arandiatierrez@aalto.fi (A. Arandia).

<https://doi.org/10.1016/j.apcatb.2022.122046>

Received 31 May 2022; Received in revised form 30 September 2022; Accepted 3 October 2022

Available online 6 October 2022

0926-3373/© 2022 The Author(s). Published by Elsevier B.V. This is an open access article under the CC BY license (<http://creativecommons.org/licenses/by/4.0/>).

(DFT) calculations and microkinetic modeling [12], under typical methanol production conditions, both CO and CO₂ hydrogenation routes can coexist.

In addition to the active discussion about the carbon source, the knowledge gained regarding the nature of the active sites in the CO₂-to-methanol (CTM) process has grown exponentially in recent decades [18–20]. CO₂ is a stable molecule and greatest difficulties in achieving great methanol selectivity in CO₂ hydrogenation are related to kinetic limitations [21]. Therefore, a molecular understanding of the key aspects that govern the activity and selectivity of a catalyst is crucial. Overall, over copper-based catalysts, the CO₂ hydrogenation to methanol reaction has been described as a structure-sensitive reaction in which not all of the surface atoms have the same role and activity [15, 18,22]. For copper-zinc oxide (Cu-ZnO) binary systems, copper is responsible for the adsorption, dissociation and spillover of atomic hydrogen (H*) [23], while zinc oxide enhances the dispersion of Cu nanoparticles and facilitates the adsorption of CO₂ [24]. The Cu-ZnO interface and surroundings have been described as the most active sites responsible for the activity wherein the intermediate species (e.g. carbonates and formates) are further hydrogenated to methanol [11, 25–27]. Lately, ZrO₂-based catalysts are emerging as active [18,28,29] and cost-effective solutions for the efficient synthesis of methanol [30] and a few experimental studies have explored the synergistic interactions of Cu/ZnO/ZrO₂ catalysts and the active interplay toward methanol production [10,18,31,32]. Alone on ZrO₂, both Cu [28,33] and ZnO [34,35] can also display some activity in the hydrogenation of intermediate species to methanol. Also, the ZrO₂/Cu inverse configuration has shown excellent properties for an efficient methanol synthesis from CO₂ [36,37].

In recent years, more investigations have described not only the synergistic effect of binary Cu/ZnO catalysts but also the effects of the locations of both the active metal (Cu) and promoter (ZnO) on methanol production from CO₂ [19,38,39]. The formation of ZnO particles or reduced Zn on the Cu surface have been found to improve the Cu dispersion and eventually, the accessible Cu surface area [11,19,25,39]. Experimental and computational studies on CO₂ hydrogenation to methanol have pointed out that the formation of ZnO aggregates on top of Cu particles promoted methanol production which may be related to the increase in the number of active ZnO-Cu pairs [19,38]. Palomino et al. [38] experimentally demonstrated that ZnO added on top of Cu (100) and (111) surfaces yields a superior methanol production compared to the inverse copper-added-on-top-of-zinc oxide catalyst. Moreover, the highest production of methanol was observed at a relatively low surface coverage (θ_{Zn}) of 0.15–0.20 monolayer (ML) and similar values of $\theta_{\text{Zn}} \approx 0.20$ ML were reported by Nakamura and coworkers for ZnO over polycrystalline copper [40], and Kattel and collaborators over Cu(111) substrates [19]. By a combination of experimental, and DFT calculations and modeling based on thermodynamics, Kuld and coworkers [41] found the highest methanol turnover frequency (TOF) at a surface coverage of $\theta_{\text{Zn}} \approx 0.47$ ML, with the TOF being greater when using larger Cu particles.

The above examples highlight the potential of and interest in synthesizing and testing zinc-on-top-of-copper catalysts with ZnO surface coverages of approximately $\theta_{\text{Zn}} \approx 0.1$ –0.2 ML. An atomic-scale synthesis technique, such as atomic layer deposition (ALD), is an efficient technique to reach this range of surface coverage. The ALD technique is based on the sequential use of self-terminating gas–solid reactions and can offer accurate atomic level control of the deposited metal concentrations [42,43]. To modify metal oxide interfaces, single atoms can be uniformly distributed on high surface area supports by ALD [43–45]. The first studies in atomic-scale synthesis (by ALD) toward CTM reaction have already been reported (e.g. ZrO₂-ALD on Cu/SiO₂ [46] and Ni-ALD on Cu nanoparticles on γ -Al₂O₃ [47]), bringing out the benefits of this technique to enhance the catalyst activity, selectivity and stability. In a recent publication, Saedy and coworkers [48] applied preferential chemical vapor deposition (PCVD) and incipient wetness impregnation

in the synthesis of ZnO/Cu/Al₂O₃ catalysts for the CTM reaction. Zinc oxide introduced by the PCVD method on a prereduced copper phase resulted in a more active and selective catalyst compared to the impregnated catalyst [48]. By means of various diffraction, spectroscopic and microscopy characterization techniques, the investigators demonstrated a more efficient production of active/selective ZnO/Cu interfaces compared to the more traditional impregnation method [48]. Furthermore, the authors suggested that the inverse ZnO/Cu interface may result in a more active system than the conventional Cu/ZnO interface [48]. In a recent research [49], ZnO was added by ALD (323 K, diethylzinc as a precursor) on copper hydroxide nanowires and the size of ZnO was tuned from isolated species to nanoparticles by increasing the number of ZnO cycles from 1 to 20. The maximum methanol production rate was found after 3 cycles.

In this work, we focused on studying the catalytic performance of diverse copper-zinc oxide on zirconia catalysts for the hydrogenation of carbon dioxide to methanol. Atomic layer deposition (ALD) and incipient wetness impregnation were applied for the incorporation of Zn and Cu into the catalyst, respectively. Zn was deposited by ALD in one ALD cycle, which in practice should correspond to atomically dispersed ZnO species covering 10–20% of the surface (0.1–0.2 ML). By alternating the order in which Cu and Zn were attached to the catalyst, we created different metal-oxide configurations. A combination of various characterization techniques, such as diffuse reflectance infrared Fourier transform spectroscopy (DRIFTS), hydrogen temperature programmed reduction (H₂-TPR), carbon dioxide temperature programmed desorption (CO₂-TPD), X-ray photoelectron and absorption spectroscopy (XPS and XAS) and scanning transmission electron microscopy-energy-dispersive X-ray spectroscopy (STEM-EDS), DFT calculations and catalytic tests, led us to identify the most active configuration. We expect that the findings of this research shall enhance the understanding of the elemental features in the zinc oxide/copper/zirconia system and help to consider the location of zinc oxide (promoter) and copper (metal) as a crucial parameter to produce active sites for the efficient hydrogenation of carbon dioxide to methanol.

2. Experimental

2.1. Preparation of copper-zinc on zirconia samples

In total, five samples were synthesized: ZnO/ZrO₂, Cu/ZrO₂, ZnO/Cu/ZrO₂, Cu/ZnO/ZrO₂ and ZnO/Cu/ZnO/ZrO₂. The self-made samples were prepared following two different methods, depending on which metal was incorporated into the porous structure of the support (monoclinic zirconia, ZrO₂). Thus, Cu was added by incipient wetness impregnation (IWI), while Zn was added by atomic layer deposition (ALD). Monoclinic zirconia, provided by Saint-Gobain NorPro as cylindrical pellets (length 5 mm, diameter 3 mm) was used as a support material (surface area of 70 m² g^{−1}). Prior to its utilization, ZrO₂ was crushed and sieved to a particle size of 250–420 μ m and calcined in a muffle furnace (Nabertherm P330) in ambient air at 873 K for 5 h (10 K min^{−1}) to remove possible surface impurities. Cu nitrate trihydrate, Cu(NO₃)₂·0.3 H₂O (CAS: 10031–43–3, Sigma Aldrich, 99–104% purity) and Zn acetylacetonate, Zn(C₅H₇O₂)₂·0.3 H₂O (Zn(acac)₂, CAS: 14024–63–6, Volatec) were used as copper and zinc precursors, respectively. The targeted areal number density for Cu and Zn was 2 atoms/nm² (Zn/Cu atomic ratio of one). The Cu and Zn loadings in wt% measured by ICP–OES are shown in Table 1, and a scheme that shows the sequence of samples prepared is shown in Fig. 1.

For the impregnation of Cu by IWI, either on ZrO₂ or ZnO/ZrO₂, the corresponding amount of Cu precursor was dissolved in the exact amount of deionized water needed to fill the pore volume of the support. The water uptake capacity of the support (≈ 0.3 mL g^{−1}) was experimentally estimated by adding deionized water drop by drop to a known amount of dried support (393 K, 24 h). Approximately 3–5 drops of the Cu nitrate solution were added at a time to an Erlenmeyer flask

Table 1

List of samples containing the metal loadings of Cu and Zn measured by ICP-OES, the corresponding areal number density of Cu and Zn (metal atoms per nm²), the amount of CO₂ desorbed determined by CO₂-TPD at 323 K and the number of reduction peaks and temperature at the maximum height of the peak determined by H₂-TPR.

Sample	Code	ICP-OES				CO ₂ -TPD			H ₂ -TPR
		Cu metal loading, wt%	Zn metal loading, wt%	Cu nm ⁻²	Zn nm ⁻²	μmol CO ₂ (g _{cat}) ⁻¹	molecules CO ₂ Zn ⁻¹	molecules CO ₂ nm ⁻²	Number of reduction peaks (temperature in K)
ZrO ₂	Zr	n.a.	n.a.	n.a.	n.a.	95	n.a.	0.8	n.a.
ZnO/ZrO ₂	Zn/Zr	n.a.	1.4	n.a.	1.9	96	0.45	0.8	n.a.
Cu/ZrO ₂	Cu/Zr	1.3	n.a.	1.7	n.a.	63	n.a.	0.5	3 (405, 418, 477)
ZnO/Cu/ZrO ₂	Zn/Cu/Zr	1.1	1.1	1.5	1.5	115	0.67	1.0	1 (418)
Cu/ZnO/ZrO ₂	Cu/Zn/Zr	1.2	1.2	1.6	1.6	85	0.45	0.7	2 (448, 500)
ZnO/Cu/ZnO/ZrO ₂	Zn/Cu/Zn/Zr	1.2	2.3	1.6	3.1	109	0.30	0.9	3 (431, 440, 475)

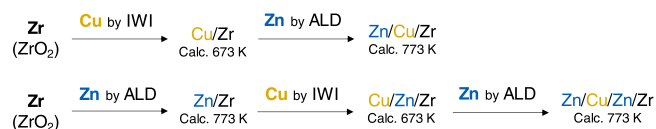


Fig. 1. Scheme of the samples synthesized and the sequence in which they were prepared. The calcination temperatures in each case were chosen for the effective removal of nitrates and (acac)₂ ligands, while minimizing the sintering of copper.

containing the dried support. Next, the partially wet support was first gently mixed, and then the flask was shaken for 2–3 min to ensure an even distribution of the solution. After adding the final drops of the solution, the slightly damp material was aged for 5 h at room temperature and dried overnight at 393 K in an oven under static air. Finally, the dried material was calcined at 673 K for 2 h (5 K min⁻¹) in a tube furnace with a constant flow of 100 mL min⁻¹ of synthetic air (AGA 99.999% purity, 20% O₂, 80% N₂).

The deposition of Zn on ZrO₂ by ALD started by treating the calcined support in a flow-type fixed bed F-120 ALD reactor (ASM Microchemistry) at 523 K for 10 h to remove moisture before the actual ALD process. Then, the solid zinc acetylacetonate reactant was vaporized at 393 K in flowing nitrogen and reacted to the pretreated ZrO₂ support by one cycle of the ALD process for 3 h at 473 K and a pressure of ca. 3 mbar. Reactant-originated acetylacetonate ligands were removed by oxidative treatment in a tube furnace in synthetic air flow (100 mL min⁻¹) at 773 K for 2 h (5 K min⁻¹). The same procedure was followed when Zn was deposited on ZrO₂, Cu/ZrO₂ and Cu/Zn/ZrO₂. Fig. 2 shows a conceptual scheme with the configurations of the various copper-zinc-zirconia catalysts that were synthesized and tested in this research.

2.2. Catalyst characterization

The metal content of the catalysts was determined by inductively coupled plasma atomic emission spectroscopy (ICP-OES). Samples (ca 0.100 mg) were weighed in Teflon vessels, and a mixture of nitric acid (HNO₃, 65%, 2.5 mL) and hydrochloric acid (HCl, 37%, 7.5 mL) was added. Vessels were closed and placed in a microwave oven (Milestone, Ethos) and heated (1 h, 200 °C). After cooling, the samples were diluted with MQ-grade water, and the Cu- and Zn-contents were determined with an F-AAS instrument (Varian 220 F) using an air-acetylene burner.

The surface area and cumulative pore volume of zirconia were obtained by nitrogen physisorption isotherm (liquid nitrogen, 77 K) in a Thermo Scientific Surfer equipment. The support sample was weighted to a quartz glass burette (ca. 200 mg) and degassed at 573 K for 3 h. Specific surface area was calculated from the isotherm according to the Brunauer-Emmett-Teller (BET) method [50]. The cumulative pore

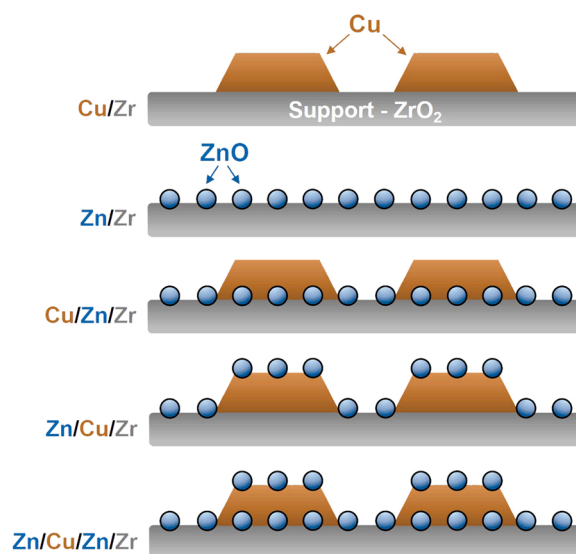


Fig. 2. Conceptual scheme of the various sample configurations prepared in this work.

volume was calculated based on the Barrett-Joyner-Halenda (BJH) method [51].

The phase/crystallinity of the support was studied by X-ray diffraction that was carried out on a ground sample in a PANalytical X'Pert Pro MPD Alpha 1 device equipped with Cu Kα1 radiation (45 kV and 40 mA). The X-ray scanning range was from 10° to 100° (2θ) with a step size of 0.0131° and a time per step of 51 s. The results are shown in the supporting information (Fig. S1). The characteristic monoclinic phase (JCPDS 37-1484) was identified with main reflections at 24.5°, 28.3°, 31.5°, 34.2°, 35.4°, 40.8°, 49.3°, 50.2°, 54.1° and 55.5°.

The reducibility of the metal oxides was studied by hydrogen temperature-programmed reduction. The experiments were performed using an Altamira AMI-200 characterization system with a thermal conductivity detector (TCD) connected to an OmniStar™ mass spectrometer (MS) produced by Pfeiffer Vacuum. A total of 150 mg of sample was placed in a U-shaped quartz reactor and treated in constant He flow (AGA 99.999% purity) at 473 K for 60 min and cooled back to 303 K. The sample was then heated from 303 to 873 K or 1173 K in 2% H₂/Ar (AGA 99.999% purity) with a heating ramp of 5 K min⁻¹. The TPR measurement of ZrO₂ and ZnO/ZrO₂ was performed up to 1173 K, while 873 K was used as the maximum temperature for the Cu-containing samples. The TPR results are qualitative (given as arbitrary units) and the areas under the peaks cannot be compared with each other. The total gas flow was set at 50 mL min⁻¹ (STP conditions) during the whole measurement.

Similarly, carbon dioxide desorption was studied by CO₂ temperature-programmed desorption. The experiments were performed using an Altamira AMI-200 characterization system with a TCD connected to an OmniStar™ MS produced by Pfeiffer Vacuum. A total of 150 mg of sample was placed in a U-shaped quartz reactor, treated in He flow at 473 K for 60 min, and cooled back to 303 K. Then, the sample was activated by heating the solid from 303 to 623 K in 2% H₂/Ar with a heating ramp of 10 K min⁻¹ and 60 min hold time. The sample was then cooled to 323 K in He flow and maintained at that temperature for 30 min. Thereafter, the reduced sample was exposed to a constant flow of 10% CO₂/He (AGA 99.999% purity) for 30 min at 323 K and flushed for 60 min at the same temperature in He flow to remove the physisorbed CO₂. Finally, the sample was heated from 323 to 1073 K in He flow to desorb the chemisorbed CO₂. The possible desorbed products were continuously monitored during the experiment by mass spectrometry. The amount of CO₂ desorbed for each measurement was quantified by using calcium carbonate (CaCO₃) as an internal standard. About 4 mg of CaCO₃ was mixed with the sample and decomposed during the desorption step into CO₂ (g) and CaO (s) in the range of 800–950 K. The total gas flow was set at 50 mL min⁻¹ (STP conditions) for all measurements.

The electronic structure of the samples was studied by high-energy-resolution fluorescence-detected X-ray absorption spectroscopy (HERFD-XAS). The experiments were performed at the ID20 beamline of the European Synchrotron Radiation Facility (ESRF, Grenoble, France) [52,53]. The beam was monochromated by a combination of a Si(111) premonochromator and a Si(311) channel-cut monochromator. The spectrometer was a von Hamos spectrometer based on three Si(333) crystal analyzers.

X-ray photoelectron spectroscopy (XPS) was used to study the surface composition of the reduced samples (623 K for 30 min, 2% H₂/Ar, transfer to XPS was done through air). The measurements were performed with a Kratos AXIS Ultra DLD X-ray photoelectron spectrometer using a monochromated AlK α X-ray source (1486.7 eV) run at 100 W. A pass energy of 80 eV and a step size of 1.0 eV were used for the survey spectra, while a pass energy of 20 eV and a step size of 0.1 eV were used for the high-resolution spectra. Photoelectrons were collected at a 90° take-off angle under ultra-high vacuum conditions, with a base pressure typically below 1 \times 10⁻⁹ Torr. The diameter of the beam spot from the X-ray was 1 mm, and the area of analysis for these measurements was 300 μ m \times 700 μ m. Both survey and high-resolution spectra were collected from three different spots on each sample surface in order to check for homogeneity and surface charge effects. All spectra were charge-corrected relative to the position of C-C bonding of adventitious carbon at 284.8 eV.

Scanning transmission electron microscopy high-angle annular dark-field (STEM-HAADF) images were acquired for the prereduced samples (623 K, 60 min, 50 mL min⁻¹ of 2% H₂/Ar, STP conditions) by a JEOL JEM-2200FS double aberration corrected, high-resolution microscope, operated at 200 kV acceleration voltage. The chemical elemental mapping analysis was conducted with an X-ray energy-dispersive spectroscopy (EDS) detector. The samples were drop-casted using acetone onto a gold grid coated with an ultrathin holey carbon film.

The evolution of the surface species during the cyclic CO₂-H₂ adsorption was measured by diffuse reflectance infrared Fourier transform spectroscopy (DRIFTS) carried out in a Nicolet Nexus FTIR spectrometer with a high temperature/pressure Spectra-Tech reactor chamber equipped with a dome and ZnSe windows. The gas flow leaving the chamber was monitored with an OmniStar GSD 301 spectrometer by Pfeiffer Vacuum. The scans were collected from 4000 to 600 cm⁻¹ at a scan resolution of 4 cm⁻¹. Prior to the experiment, a background spectrum was acquired under room conditions using an aluminum mirror in constant Ar flow. Approximately 20 mg of crushed sample powder was placed in the sample holder, heated from room temperature to 673 K in a constant flow of 10% O₂/N₂/Ar (synthetic air: AGA 99.999% purity, 20% O₂, 80% N₂; Ar: AGA 99.9999% purity) and kept there for 60 min

to remove possible surface impurities. The temperature was then decreased to 623 K in the same atmosphere, and the gas was switched to 10% H₂/Ar (H₂: AGA 99.999% purity; Ar: AGA 99.9999% purity) and kept for 60 min to activate the metal oxides. The catalyst was then cooled to the desired reaction temperature, either 450, 500 or 550 K, and flushed with Ar for 30 min. The cyclic adsorption of CO₂-H₂ consisted of three consecutive full cycles of the following sequence: i) CO₂ adsorption for 12 min under flowing 10% CO₂/He (AGA 99.999% purity), ii) switching to Ar flow for 12 min, iii) switching to H₂ adsorption for 12 min under flowing 10% H₂/Ar and, iv) switching to Ar flow for 12 min. During each step within each cycle, a spectrum (100 scans, approximately 2 min) was recorded at 0, 5 and 10 min to monitor the surface of the catalyst with respect to time on stream. The total gas flow was set at 50 mL min⁻¹ (STP conditions) during the whole experiment. A summary of the experimental conditions (timing, gases, flow rates, and temperatures) used for DRIFTS experiments is depicted in Fig. 3.

2.3. Computational methods

To assist infrared band identification, density functional theory (DFT) calculations were performed using the BEEF-vdW exchange-correlation functional [54] as implemented in the GPAW [55] software. The monoclinic zirconia was described by a two-layer-thick slab model, built from a 3 \times 2 m-ZrO₂(111) supercell with periodic boundary conditions used in the lateral directions. The final cell measurements were 20.67 \times 14.79 \times 24.0 Å with angles of 90°/90°/116.5°. Cu(111) and stepped Cu(110) surfaces were modeled as three-layer periodic slabs, where the bottom layers were kept fixed in their bulk geometry in unit cells of 4 \times 4 and 3 \times 4, respectively. The core electrons of all elements were described by projector-augmented wave (PAW) [56] setups in the frozen-core approximation. A real-space grid basis was used with a maximum grid spacing of 0.2 Å. Periodic boundary conditions were used in two directions and the reciprocal space was sampled at the Γ point. A Hubbard U correction [57] of 2.0 eV was applied to the d-orbitals of the zirconium atoms. The atomic structures were optimized using the Fast Inertial Relaxation Engine (FIRE) algorithm as implemented in the Atomic Simulation Environment (ASE) [58,59] package until the maximum residual force was below 0.005 eV Å⁻¹. Vibrational frequencies for modes involving adsorbate and binding catalyst surface atoms were determined using the Frederiksen method [60]. The frequencies of the combined modes were obtained by adding up the frequencies of their individual contributions.

2.4. Activity tests in a continuous flow reactor

The catalytic performance was evaluated in a high-pressure continuous-flow fixed-bed equipped with a stainless-steel tube reactor with a mesh placed in the midsection of the reactor. One gram of calcined catalyst, sieved to 0.25–0.42 mm, was loaded in the reactor. Prior to the catalytic reaction, the catalyst was activated by in situ reduction at 623 K for 60 min with a constant flow of 10% H₂/N₂ (v/v; H₂: AGA 99.999% purity, N₂: AGA 99.999% purity). Activity tests were conducted at 450, 500 and 550 K with a total pressure of 3.0 MPa and a gas hourly space velocity (GHSV) of 7500 h⁻¹ (STP conditions: 273.15 K and 1 bar). The reaction mixture was composed of H₂/CO₂/N₂ (~ 71/23/6, v/v/v; H₂: AGA 99.999% purity; CO₂: AGA 99.995%; N₂: AGA 99.999% purity). The volumetric flows were 6.3 L h⁻¹ of H₂, 2 L h⁻¹ of CO₂ and 0.6 L h⁻¹ of N₂ (STP conditions) and the volume of catalyst used per experiment was approximately 1.2 \times 10⁻³ L. For each catalyst, the reaction temperature was increased in steps of 50 K. Initially, the reactor temperature was stabilized at 450 K and kept there for 90 min. Next, the temperature was increased to 500 K (10 K min⁻¹), stabilized, and kept there for another 90 min. Finally, the procedure was repeated for the highest temperature of 550 K. Thus, the data depicted in this manuscript were collected after 90 min under each operating condition. The unreacted gases and reaction products were continuously monitored

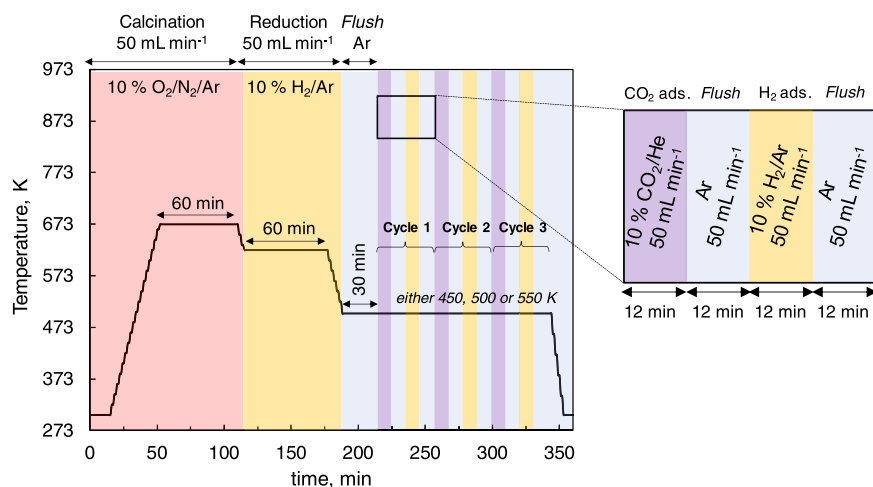


Fig. 3. Summary of the timing and experimental conditions used for the DRIFTS experiments. Heating and cooling ramps are estimates.

in an Agilent 490 Micro Gas Chromatograph (microGC) fitted with a thermal conductivity detector (TCD) and equipped with two columns: a) MS-5 molecular sieve for permanent gases H_2 , N_2 , CH_4 and CO and, b) PorapLOT U for CO_2 , CH_3OH and H_2O . The CO_2 conversion (X_{CO_2} , Eq. 1) and product selectivity (S_i , Eq. 2) were calculated by internal

normalization standard with N_2 . The CO_2 conversion, the selectivity of CH_3OH , CO and CH_4 and the space-time yield of CH_3OH (STY_{CH_3OH} , $mmol\ h^{-1}\ g_{cat}^{-1}$, Eq. 3) were calculated according to the following formulas:

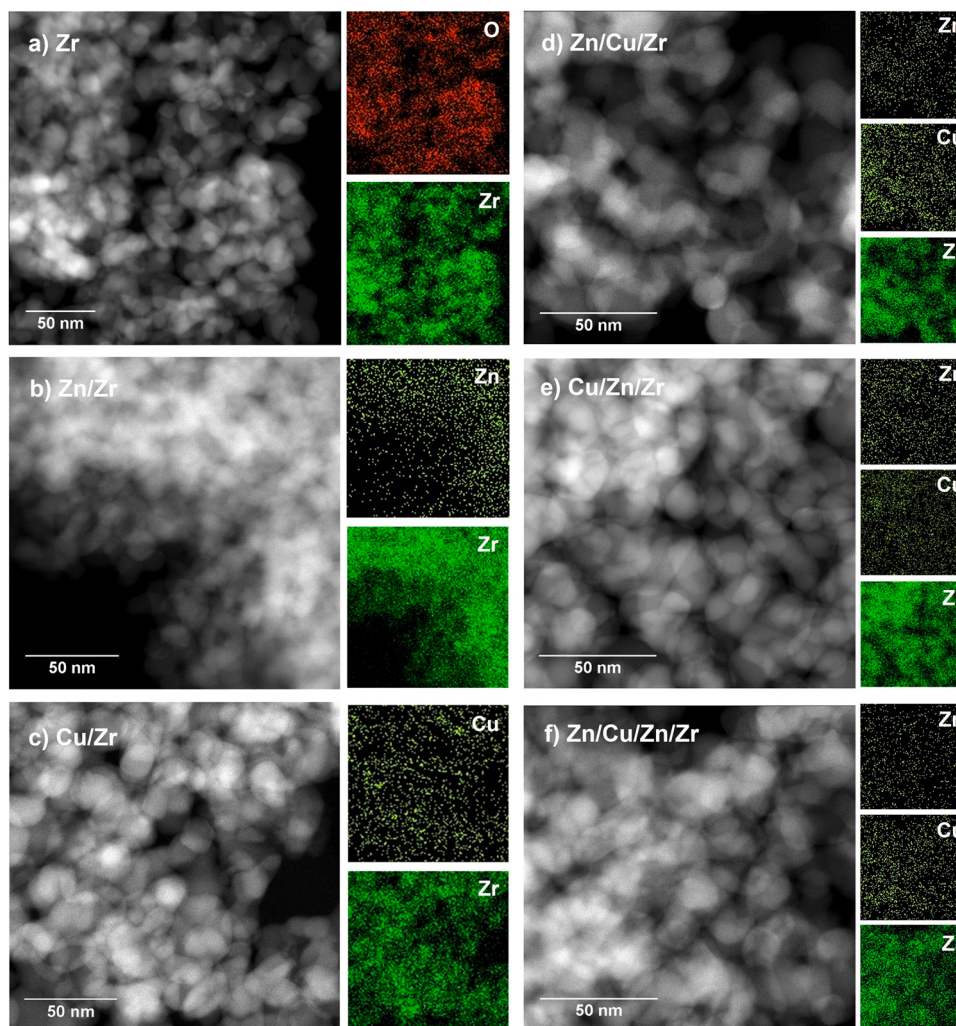


Fig. 4. STEM-HAADF images and energy-dispersive X-ray spectroscopy (EDS) mapping of different elements for Zr (a) and prereduced Zn/Zr (b), Cu/Zr (c), Zn/Cu/Zr (d), Cu/Zn/Zr (e) and Zn/Cu/Zn/Zr (f) samples.

$$X_{\text{CO}_2}(\%) = \frac{F_{\text{CO}_2, \text{in}} - F_{\text{CO}_2, \text{out}}}{F_{\text{CO}_2, \text{in}}} * 100\% \quad (1)$$

$$S_i(\%) = \frac{F_{i, \text{out}}}{F_{\text{CH}_3\text{OH}, \text{out}} + F_{\text{CO}, \text{out}} + F_{\text{CH}_4, \text{out}}} * 100\% \quad (2)$$

$$STY_{\text{CH}_3\text{OH}}(\text{mmol h}^{-1} \text{g}_{\text{cat}}^{-1}) = \frac{F_{\text{CO}_2, \text{in}} * X_{\text{CO}_2} * S_{\text{CH}_3\text{OH}}}{m_{\text{cat}}} \quad (3)$$

where F_{CO_2} and F_i are the molar flow rates of CO_2 or products (CH_3OH ,

CO and CH_4) and m_{cat} is the mass of catalyst in grams.

3. Results and discussion

3.1. Characterization of fresh catalysts

The list of samples (support and self-made catalysts), the corresponding sample code used throughout the manuscript, the Cu and Zn metal loadings measured by ICP-OES and the Cu and Zn areal number density, the amount of CO_2 desorbed in the CO_2 -TPD experiments and

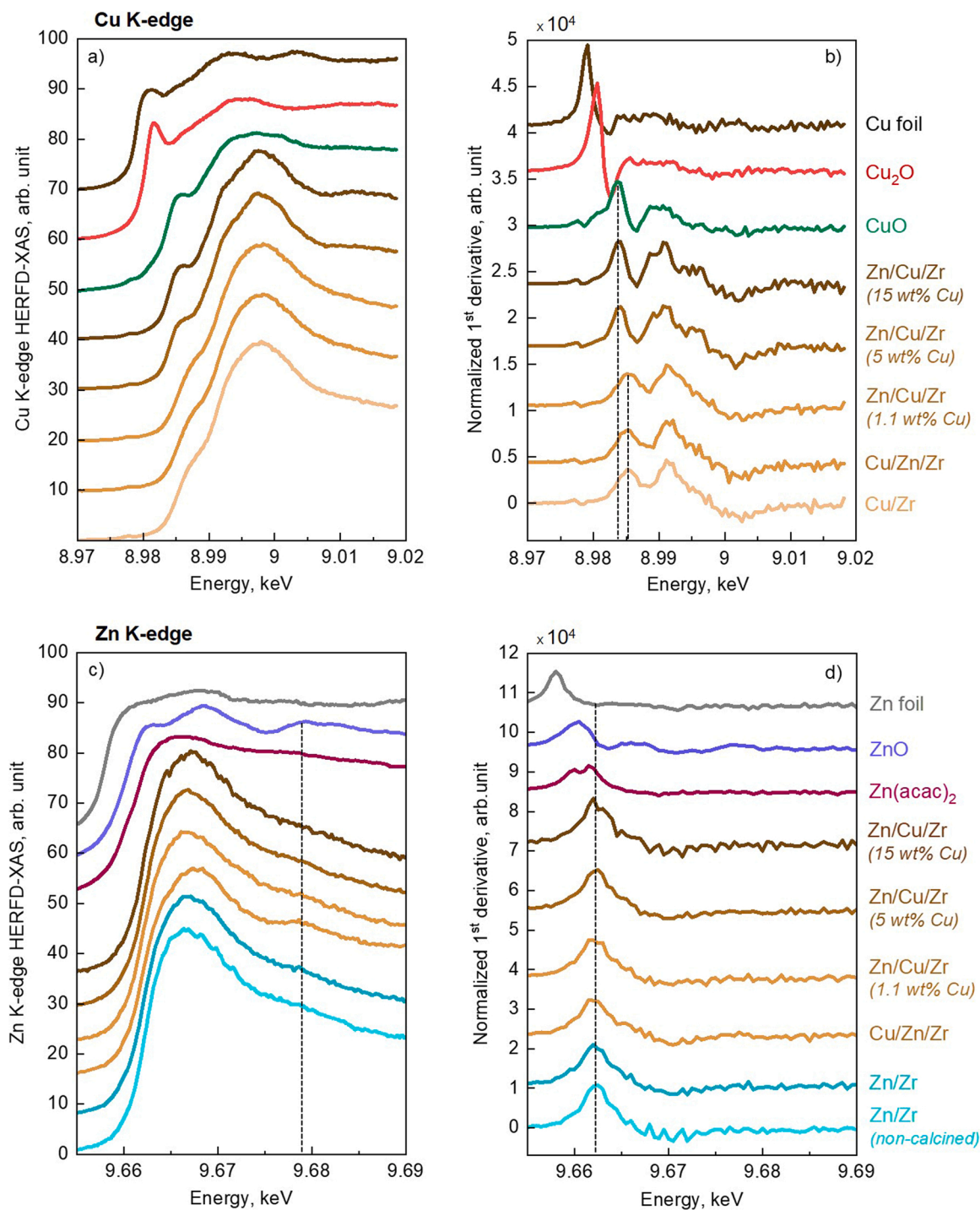


Fig. 5. Cu K-edge HERFD-XAS (a) and normalized first derivative (b) and, Zn K-edge HERFD-XAS (c) and normalized first derivative (d) for the self-made Cu-Zn on ZrO_2 samples. Cu foil, Cu_2O , CuO, Zn foil, ZnO and $\text{Zn}(\text{acac})_2$ spectra were included as references.

the number of reduction peaks (for Cu-species) and temperature at the maximum height of the peak determined by H₂-TPR are listed in Table 1.

The STEM-HAADF images and EDS mapping of elements for the support and self-made samples are depicted in Fig. 4. Based on the results, the elements mapped for each sample seem to be evenly distributed throughout the samples and no high concentration spots were detected in any of the samples. The estimation of the Cu and Zn particle size distributions was impossible due to the poor contrast between Cu, Zn and Zr.

Also, the percentage of a monolayer of ZnO (% ML) was estimated as a ratio between the areal number density of ZnO in each sample (Zn atoms per nm², calculated from the Zn metal loadings measured by ICP-OES) and the average areal number density of Zn in one bulk ZnO monolayer obtained through equation reported elsewhere [42] (12.0 nm⁻², from ZnO density = 5.61 g cm⁻³). According to these calculations, one Zn-ALD cycle (Zn/Zr, Cu/Zn/Zr and Zn/Cu/Zr samples) yielded approximately 15% of a bulk ZnO ML equivalent.

3.2. X-ray absorption spectroscopy (XAS)

The electronic structure (oxidation states) of copper and zinc was investigated by high-energy-resolution fluorescence-detected X-ray absorption spectroscopy (HERFD-XAS). The Cu and Zn absorbance at the Cu and Zn K-edges are depicted in Fig. 5 for the various catalysts and references (Cu foil, Cu₂O, CuO, Zn foil, ZnO and Zn(acac)₂). Along with the samples prepared and reported in Table 1, two more samples were prepared and analyzed: Zn/Cu/Zr (5 wt% Cu) and Zn/Cu/Zr (15 wt% Cu). These samples were synthesized to observe a possible effect of the Cu loading on the electronic structure of Cu and Zn. All the samples analyzed by HERFD-XAS were studied after the calcination treatment detailed under Section 2.1 (673 K or 773 K when Cu or Zn were added last, respectively), except a Zn/Zr sample that was also studied before the calcination step, i.e., after the Zn-ALD cycle.

Analyzing the Cu K-edge HERFD-XAS and first derivative (relative to incident energy) spectra (Fig. 5a-b) of the Zn/Cu/Zr samples with various Cu loadings, the spectra of the samples with 5 wt% and 15 wt% Cu were similar to that of CuO, which indicated a clearer presence of bulk CuO when increasing the Cu content. The characteristic edge transition for CuO can be observed at ca. 8.984 keV [32]. The rest of the samples (Zn/Cu/Zr with 1.1 wt% Cu, Cu/Zn/Zr and Cu/Zr) showed the absence of the first main shoulder that caused an apparent shift of the first peak of the derivative spectrum toward higher energies (Fig. 5b). The shoulder in CuO stems from 1 s to 4p transitions with a charge transfer from the ligand (1s13d10 L₁ final state, with L₁ denoting a ligand hole) [61,62]. This ligand effect decreases from CuO to the catalysts and it is typically absent in tetrahedral Cu(II) complexes [63]. The local coordination in bulk CuO is nearly square planar while the difference in the catalysts indicates a different local coordination in the surface-dominated Cu species. Thus, the pre-edge intensity (at 8.979 eV) decreases from CuO to the catalysts, indicating more likely an octahedral coordination in our samples, where the pre-edge is dipole-forbidden. However, the absence of the characteristic Cu¹⁺ 1 s-4p transition feature at ca. 8.98 keV [63] indicates the absence of Cu₂O in any of the samples. Thus, it can be concluded that the Cu valence state seemed to be Cu²⁺ for all the catalysts.

For the Zn K-edge (Fig. 5c-d), the HERFD-XAS spectra and 1st derivative were very similar for all the samples, which suggests that the chemical environment for Zn is not significantly influenced either by the order in which Cu and Zn were added to the catalyst or by the Cu loading. Comparing the HERFD-XAS spectra of the samples with the ZnO (wurtzite) reference, there were significant differences; however, the presence of the Zn²⁺ oxidation state can be assumed. The peak at 9.679 eV present on ZnO reference, assigned to multiple scattering on atomic neighbors beyond the first shell [64], was not visible in any of the samples (except for a small peak observed on the Cu/Zn/Zr sample) which evidenced the presence of atomically dispersed ZnO species. It

was computationally [64] and experimentally [49] demonstrated that ZnO XANES features are developed while increasing the number of ZnO atomic shells and, consequently, the ZnO cluster size. To the best of our understanding, it was expected that Zn was atomically dispersed as lone ZnO units with an oxidation state of Zn²⁺.

3.3. X-ray photoelectron spectroscopy (XPS)

To complement the bulk structural-chemical information obtained by HERFD-XAS, the surface composition was analyzed by XPS. The samples were reduced ex situ and momentarily exposed to the atmosphere during the preparation before the analysis.

The elemental composition and the relative amount of the diverse zinc components are included in Table 2. The survey spectra of the samples in the range of 0–1200 eV are included in Fig. S2 and the high-resolution XPS spectra of the Zn 2p and Cu 2p regions are depicted in Fig. 6. As expected, all samples exhibited zirconium and oxygen, the relative amount of which decreased when adding other components (Table 2). The surface concentration of copper and zinc content measured by XPS varied between 2–4 and 3–7 at%, respectively, for the samples. The Zn/Cu atomic ratio was close to two for the samples with one ALD cycle of Zn and Cu by impregnation. Compared to the bulk atomic ratio of about one (see Table 1), the observed Zn/Cu ratio is consistent with zinc located on the surface and copper somewhat clustered. Addition of zinc on Cu/Zr decreased the surface concentration of copper, as expected (from 3.0 to 1.9 at% for Zn/Cu/Zr). According to XPS, the Cu/Zn/Zr sample had a higher surface concentration of both copper and zinc than the inverse Zn/Cu/Zr. While the reason for this observation is not fully clear, we speculate that it may have to do with the details of impregnation (zinc oxide is amphoteric [65] and the impregnation solution was acidic; part of the zinc may have dissolved and migrated to the outer surface during drying). Addition of zinc on Cu/Zn/Zr again decreased the surface concentration of copper (from 4.0 to 2.8 at% on Zn/Cu/Zn/Zr).

Taking a closer look at the high resolution XPS results, the Zn 2p_{3/2} region (Fig. 6a) could be deconvoluted to three different species of Zn²⁺. These correspond to ZnO-like species (1021.5 eV) and Zn mixed state denoted *a* (1023.1 eV) and Zn mixed state denoted *b* (1024.4 eV). The presence of metallic zinc can be discarded due to the absence of a peak at a slightly lower binding energy (at ~ 1021 eV [66]). The highest fraction of zinc in ZnO-like species was in the Zn/Cu/Zr sample (over 85%). The Cu 2p_{3/2} region (Fig. 6b) showed the presence of Cu metal (Cu⁰) and Cu²⁺ in all Cu-containing samples. Although the samples had been reduced before the XPS measurements, sample transfer through air to XPS had evidently been sufficient to oxidize part of the Cu⁰ to Cu²⁺.

Table 2

XPS-measured relative surface concentration of elements and relative amount of the different components of zinc.

Sample	Element, at% ^a					Zn/ Cu ratio	Components of zinc, %	
	Zr 3d	Zn 2p	Cu 2p	O 1 s	C 1 s		ZnO	Zn mixed state <i>a</i> + <i>b</i>
Zr	31.9	0.0	0.0	53.7	12.6	–	0.00	0.00
Zn/Zr	30.6	2.9	0.0	52.8	12.5	–	69.8	27.4 + 2.8
Cu/Zr	30.9	0.0	3.0	51.6	13.6	–	0.00	0.00
Zn/Cu/ Zr	28.3	3.6	1.9	51.2	14.3	1.9	86.7	12.5 + 0.8
Cu/Zn/ Zr	23.1	7.1	4.0	50.1	15.3	1.8	72.3	22.2 + 5.5
Zn/Cu/ Zn/Zr	25.3	7.0	2.8	49.4	14.9	2.5	73.0	21.8 + 5.2

^a The remaining percentage in the elemental composition up to 100% corresponds to a small contamination of fluorine.

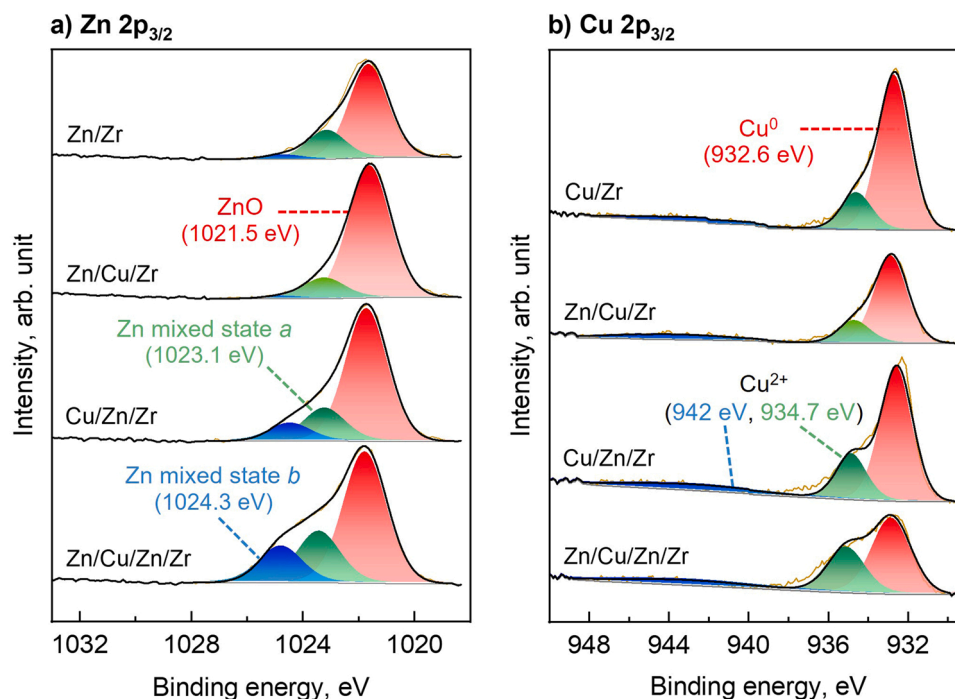


Fig. 6. High-resolution XPS spectra of the Zn 2p (a) and Cu 2p (b) regions for the self-made Cu-Zn on zirconia samples.

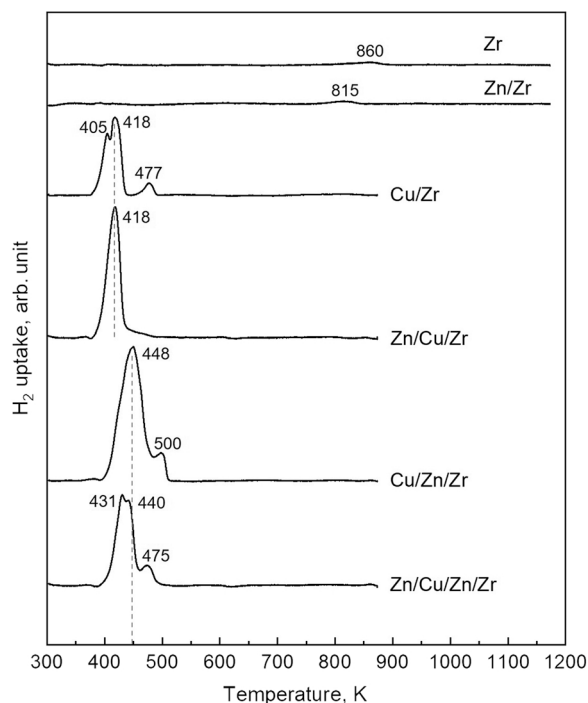


Fig. 7. Temperature-programmed reduction (H₂-TPR) profiles of zirconia support (Zr) and self-made Cu-Zn on zirconia samples. The samples are described in Table 1.

3.4. Temperature-programmed experiments

The reducibility of CuO was studied by H₂-TPR (hydrogen temperature-programmed reduction). The results are shown in Fig. 7. The reduction profiles for Zr and Zn/Zr samples are also shown in Fig. 7 as a reference. The Zr sample showed a very small and broad reduction peak with a maximum at 860 K that can be related to the formation of

surface oxygen vacancies on the support [67,68]. On the Zn/Zr sample, a single reduction peak was found at 815 K, which can be associated with the partial reduction of the support and/or with the partial reduction of ZnO to metallic Zn [69,70].

The Cu-containing samples showed various reduction peaks in the range of 360–510 K, depending on the order in which Cu and Zn were incorporated into the support. Reduction of CuO in the Cu/Zr sample generated up to three reduction peaks: two overlapping peaks with maxima at 405 and 418 K and a third peak with a maximum at 477 K. The double reduction peak at relatively low temperatures (frequently named the α and β peaks [71–74]) has been previously reported in samples with relatively low CuO loadings of approximately 5 wt%. In accordance with these authors, well-dispersed Cu²⁺ species are first reduced to Cu⁺ (α -peak) and subsequently to Cu⁰ (β -peak). The third peak at higher temperature can be assigned to the reduction of more poorly dispersed bulk-like CuO particles or CuO particles with a stronger metal-support interaction [72,73,75].

The deposition of Zn on top of Cu/Zr (Zn/Cu/Zr sample) led to a partial improvement in the reducibility of CuO. The previously reported α and β peaks in the Cu/Zr sample merged into a single reduction peak at 418 K, while the reduction at 477 K in Cu/Zr shifted to a lower temperature. This latter observation suggests that the addition of Zn after Cu improved the dispersion of bulk CuO particles [19,76]. Surprisingly, when zinc was added by ALD before copper impregnation (Cu/Zn/Zr sample), higher reduction temperatures than in the Zn/Cu/Zr sample were observed with two reduction peaks at ca. 448 and 500 K, the latter presumably generated by the reduction of larger CuO particles. The positive effect of zinc addition after copper impregnation on the reducibility of bulk CuO is also observable in the Zn/Cu/Zn/Zr sample with a shift of the peak maximum from 500 to 475 K.

The CO₂-TPD (carbon dioxide temperature-programmed desorption) profiles of pure Zr and the self-made Cu-Zn on Zr samples are displayed in Fig. 8. Up to four different desorption peaks or desorption domains can be identified. The first two peaks (at ca. 380 and 445 K) can be assigned to weakly basic sites with different gas–solid interactions, while peaks at approximately 565 and 700 K can be attributed to moderate and strong basic sites, respectively [77,78]. Accordingly, the

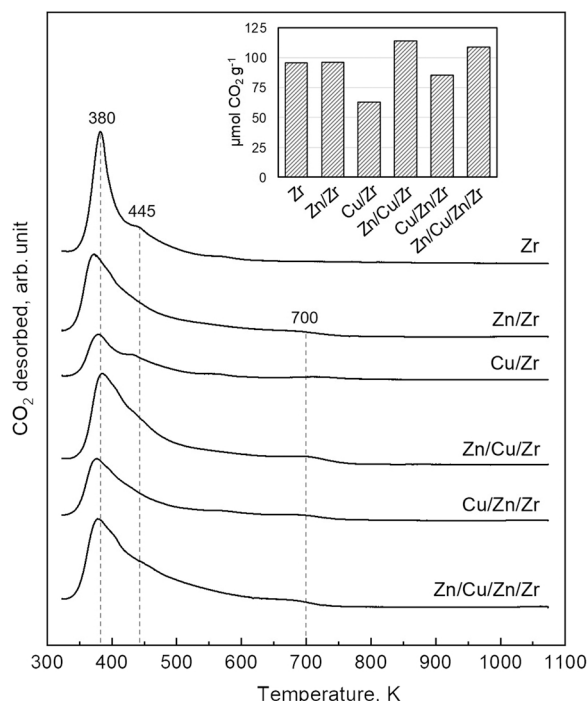


Fig. 8. Temperature-programmed desorption (CO₂-TPD) profiles of zirconia (Zr) support and self-made Cu-Zn on zirconia samples. The bar chart in the upper right corner shows the amount of CO₂ desorbed per gram of catalyst calculated with an internal standard (CaCO₃). The samples are described in Table 1.

desorption profile of pure Zr showed the presence of a significant amount of desorbed CO₂ in the range of 340–600 K with a main desorption peak at 380 K (most likely bicarbonate species on surface -OH groups) and a less significant and broader peak at 445 K. The addition of Cu and/or Zn resulted in the appearance of new desorption peaks at higher temperatures while the main peak at approximately 380 K became broader and less intense.

The amount of desorbed CO₂ (Table 1) followed the order (from higher to lower): Zn/Cu/Zr > Zn/Cu/Zn/Zr > Zn/Zr > Zr > Cu/Zn/Zr > Cu/Zr ranging from 115 to 63 μmol of CO₂ per gram of catalyst. In general, ZnO played an important role for the adsorption of CO₂, especially when it was introduced after copper. The deposition of ZnO on Cu/Zr sample (Zn/Cu/Zr sample) increased the total amount of adsorbed CO₂ from 63 to 115 μmol CO₂ g_{cat}⁻¹ (~80% higher) while the deposition of ZnO on Cu/Zn/Zr (Zn/Cu/Zn/Zr sample) increased the adsorbed CO₂ from 85 to 109 μmol CO₂ g_{cat}⁻¹ (~30% higher). This trend shows the benefits of the zinc-after-copper pair in promoting the adsorption capacity of the catalyst and the advantages of adding the Zn atoms after Cu. When the results were expressed as molecules of CO₂ per Zn atom (Table 1), Zn/Cu/Zr was still a superior catalyst (0.67 molecules of CO₂ per Zn atom); however, the Zn/Cu/Zn/Zr sample performed worse, turning out to be the catalyst with the lowest capacity among the Zn-containing catalysts (0.3 molecules of CO₂ per Zn atom). These results showed that Zn has an essential role in the adsorption of CO₂ but the amount of CO₂ and the Zn loading are not linearly correlated, the Zn/Cu/Zr being the preferred configuration to maximize the amount of adsorbed CO₂.

3.5. Evaluation of CO₂ and H₂ adsorption by DRIFTS

To understand the CO₂ and H₂ adsorption of Cu and Zn on ZrO₂, the surface species were monitored during three consecutive adsorption cycles of CO₂ and H₂ by in situ DRIFTS. To follow the catalyst surface with the experiment, representative spectra of the first and third cycles

of adsorption are depicted in Fig. 9 in the fingerprint region (1700–1200 cm⁻¹). The results are shown for the studied catalysts at three temperatures (450, 500 and 550 K). The selected spectra in Fig. 9 show the surface species after either 5 or 10 min of a certain gas flow (CO₂, H₂ or Ar). In the supplementary material (Figs. S3–S7), monitoring with respect to time on stream (first five minutes of exposure to CO₂ and H₂) of the surface species during the first cycle of CO₂ and H₂ adsorption is displayed. An example of the evolution of several MS signals during the DRIFTS experiment carried out at 500 K with the Zn/Cu/Zr sample is displayed in Fig. S8.

The cyclic adsorption on the Zr sample (Fig. 9a) was considered to serve as a reference for the CO₂ and H₂ adsorption capabilities of the support material at various temperatures. After 10 min of CO₂ flow, the surface showed the presence of bicarbonate species, HCO₃⁻ at ca. 1625, 1427 and 1220 cm⁻¹ and bidentate carbonates CO₃²⁻ at ca. 1560–1530, and 1330 cm⁻¹, with the band positions exhibiting good agreement with the literature [79–82]. According to the literature, the presence of terminal -OH groups is required for the formation of bicarbonate species, while carbonates (either monodentate, bidentate or polydentate) require the presence of coordinately unsaturated (c.u.s.) Zr⁴⁺ and O²⁻ sites [79,80,82]. Experimentally, the highest intensity for bicarbonate species was observed at the lowest temperature (450 K), and the intensity decreased with increasing temperature, especially from 450 to 500 K. In contrast, the intensity of bidentate carbonate species was not significantly affected by the temperature of the experiment. The spectrum after one minute of CO₂ flow (Fig. S3) did not differ from the spectrum after 10 min, which indicated a rapid saturation of the surface with carbonate and bicarbonate species. After switching the gas flow from CO₂ to Ar, bicarbonate species vanished almost completely during 10 min of Ar purge. At 450 K, vibrational bands at ca. 1564 and 1330 cm⁻¹ corresponding to bidentate carbonate species remained slightly visible, which suggested a stronger adsorption of these species to ZrO₂ compared to bicarbonate species. A similar observation was made by Kouva and coworkers [79] when studying the adsorption of CO₂ on ZrO₂ by DRIFTS in the range of 373–673 K. Both the first and third cycles of adsorption yielded comparable spectra with no apparent accumulation of any species throughout the experiment.

The incorporation of Zn atoms onto ZrO₂ by ALD (Zn/Zr sample, Fig. 9b) clearly modified the CO₂ adsorption capacity of ZrO₂. After 10 min of CO₂ exposure (either during the first or third cycle of adsorption), a crowded carbonate region (1600–1300 cm⁻¹) was observed. The vibrational band at 1220 cm⁻¹ during the CO₂ flow indicated the presence of bicarbonate species, most likely on unsaturated Zr or Zn sites [83,84]. After 10 min of Ar purge after the first cycle of CO₂ adsorption, the spectra still displayed a busy carbonate region, indicating that Zn or the Zn-ZrO₂ interface can store CO₂-related species (especially carbonates at ca. 1535 cm⁻¹) with a greater adsorption strength than ZrO₂. The switch from Ar to H₂ flow led to the formation of new species such as formates (*HCOO⁻) located at ca. 2966, 2873 (Fig. S4), 1575, 1379 and 1365 cm⁻¹ (Fig. 9b), while the intensity of carbonate species (at ca. 1535 cm⁻¹) decreased in parallel. The formation of formate species was already visible after 1 min of H₂ flow (Fig. S4), which indicated a speedy hydrogenation of carbonates to formates on a Zn/Zr sample. In addition, more formates were clearly detected with increasing experimental temperature and number of adsorption cycles. This indicated: i) the ability of the Zn or Zn-ZrO₂ interface to accumulate carbonates during the CO₂ flow and to further convert them to formates, and ii) the high stability of formates on the Zn/Zr sample even at high temperature since they did not disappear or further react between cycles.

The computational and experimentally observed infrared vibrational frequencies for formate species are displayed in Table 3. The frequencies for formate species were computed on different model systems such as m-ZrO₂ (111), ZnO/m-ZrO₂ (111), Cu (111), and Cu (110). The model surfaces used in DFT calculations are displayed in Fig. S9. Additionally, the computed IR frequencies for possible intermediates, such as formic

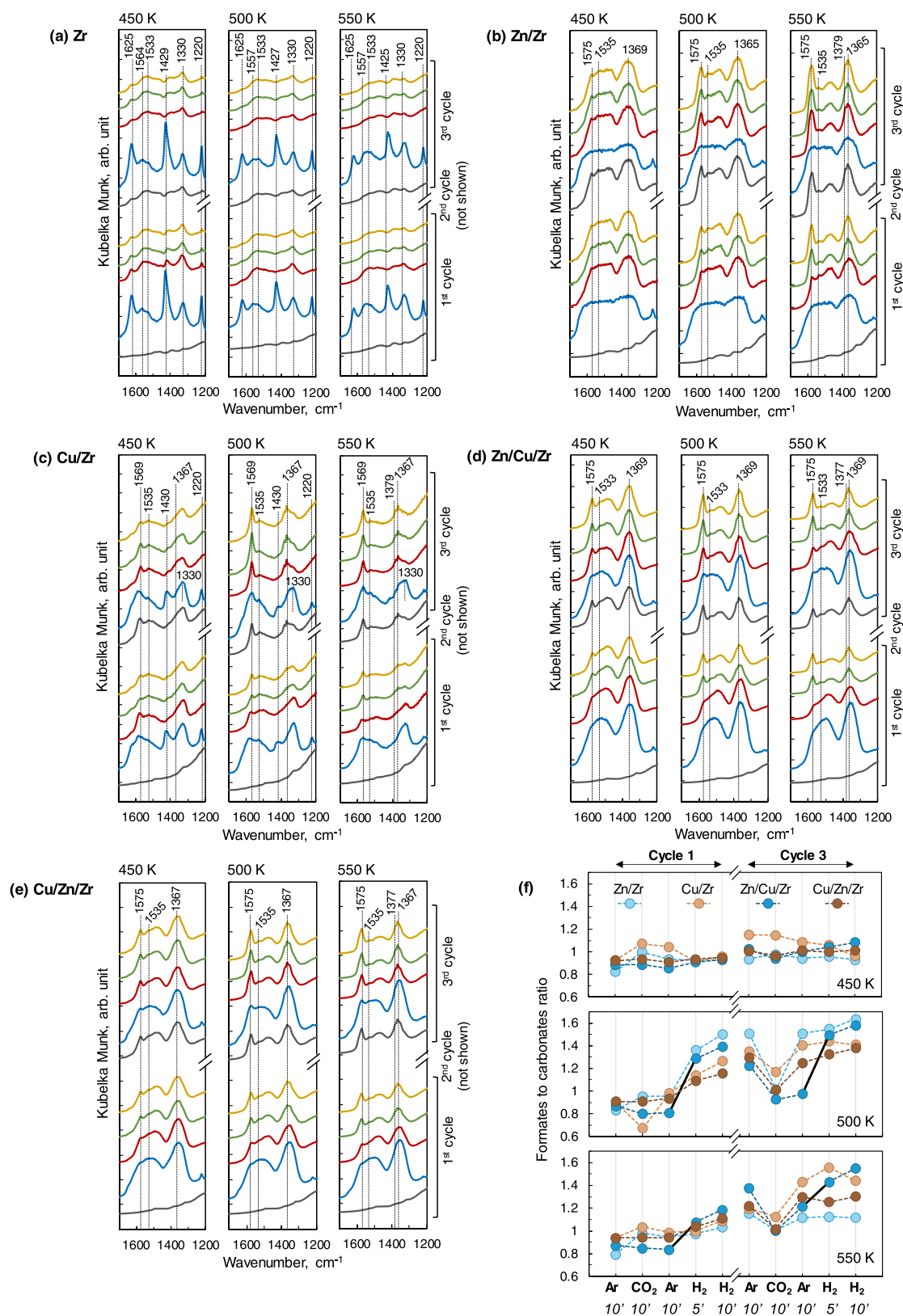


Fig. 9. DRIFT spectra of surface species in the 1700–1200 cm⁻¹ (fingerprint) region during the 1st and 3rd cyclic adsorption of CO₂-H₂ with Ar purge in between for (a) Zr, (b) Zn/Zr, (c) Cu/Zr, (d) Zn/Cu/Zr and (e) Cu/Zn/Zr samples. Color coding: in Ar flow before switching to CO₂ flow (gray), after 10 min of CO₂ flow (blue), after 10 min Ar flow before switching to H₂ flow (red), after 5 min of H₂ flow (green), after 10 min of H₂ flow (yellow). (f) Formates (ca. 1575 cm⁻¹) to carbonate (ca. 1335 cm⁻¹) intensity ratio for each catalyst and different temperatures. Experimental conditions: 0.1 MPa; 450, 500 and 550 K; 50 mL min⁻¹ (STP conditions) of: Ar during Ar purge; 10% CO₂/He during CO₂ flow; 10% H₂/Ar during H₂ flow. The results for the 1st and 3rd cycle of adsorption are presented.

Table 3

Comparison between experimental and DFT calculated infrared vibrational frequencies (in cm^{-1}) for formate species. Formates were calculated for m-ZrO₂, ZnO/m-ZrO₂, Cu (111) and Cu (110) systems.

Assignment	Experimental IR frequencies (cm^{-1})	Calculated IR frequencies (cm^{-1})			
		m-ZrO ₂	ZnO/m-ZrO ₂	Cu (111)	Cu (110)
OCO-symmetric, $\nu_s(\text{O-C-O})$	Zn/Zr: 1365–1369				
	Cu/Zr: 1367				
	Zn/Cu/Zr: 1369	1323	1326	1307	1315
	Cu/Zn/Zr: 1367				
CH swing, bending $\delta(\text{C-H})$	Zn/Zr: 1379				
	Cu/Zr: 1379				
	Zn/Cu/Zr: 1377	1338	1358	1347	1358
	Cu/Zn/Zr: 1377				
OCO-asymmetric, $\nu_{as}(\text{O-C-O})$	Zn/Zr: 1575				
	Cu/Zr: 1569				
	Zn/Cu/Zr: 1575	1532	1535	1507	1524
	Cu/Zn/Zr: 1575				
CH stretch, $\nu(\text{C-H})$	Zn/Zr: 2869				
	Cu/Zr: 2873				
	Zn/Cu/Zr: 2867	2981	2961	2970	2953
	Cu/Zn/Zr: 2869				

acid *HCOOH, carboxyl *COOH and dioxymethylene *H₂COO, which are intermediate species in methanol formation [19,85], are given in Figs. S10–S13. According to the DFT calculations, formate species produced four different bands on ZnO/ZrO₂ in the 3000–1200 cm^{-1} region that correspond to different functional groups and types of vibration. The bands were located at 1326, 1358, 1535 and 2961 cm^{-1} , and they correspond to symmetric stretch $\nu_s(\text{O-C-O})$, bending $\delta(\text{C-H})$, asymmetric stretch $\nu_{as}(\text{O-C-O})$ and stretching $\nu(\text{C-H})$, respectively. The experimental band at ca. 2970 cm^{-1} can be attributed to the combination of C-H bending and asymmetric O-C-O stretching modes [86].

The first cycle of CO₂ adsorption over the Cu/Zr sample (Fig. 9c) led to a less crowded fingerprint region compared to Zn/Zr sample. As for the Zr sample, the main species detected were bicarbonates (at ca. 1625, 1430 and 1220 cm^{-1}) and bidentate carbonates (at ca. 1557 and 1330 cm^{-1}): the bicarbonates were rapidly removed after 10 min of Ar purge. Additionally, according to the band observed at 1535 cm^{-1} , carbonates were present on the catalyst surface. Similar to the Zn/Zr sample (Fig. 9b), formates were formed during exposure to H₂; however, the position of the band of the O-C-O asymmetric vibration differed (1575 cm^{-1} on the Zn/Zr sample and 1569 cm^{-1} on the Cu/Zr sample). A lower IR frequency for formate species on Cu (111 and 110) compared to that on a Zn/Zr sample was also predicted by DFT calculations (Cu (111) vs. ZnO/m-ZrO₂, Table 3). After three consecutive cycles of CO₂ and H₂ adsorption, formates reached the highest intensity at 500 K, followed by 550 and 450 K. During the 3rd cycle of H₂ flow on the Cu/Zr sample, the intensity of formate species slightly decreased from 5 to 10 min on stream, which evidenced the strong adsorption of formate species on the Cu/Zr sample. Herein, by using a combined experimental and computational (DFT calculations) approach, Larmier and coworkers [85] found that on a Cu/ZrO₂ catalyst, formate species exhibit a low Gibbs free energy, which dictates their strong adsorption on the catalyst surface.

With Zn/Cu/Zr (Fig. 9d) and Cu/Zn/Zr (Fig. 9e) samples, the detected species and the discussed trends with respect to temperature and CO₂ and H₂ cycles displayed a combination of the results observed based on Zn/Zr and Cu/Zr samples. Thus, mainly due to the presence of Zn in both Zn/Cu/Zr and Cu/Zn/Zr samples, the fingerprint region was highly occupied by CO₂-related species after exposing the catalysts to CO₂. Formate was the main species detected after completing the cycles of adsorption of CO₂ and H₂, and no further hydrogenated species were observed (such as formic acid, *HCOOH, dioxymethylene, *H₂COO or methoxy, *H₃CO).

Based on the DRIFTS results discussed above, carbonates were

present on all samples, and formate was the prevalent hydrogenated species in the selected experimental conditions. To compare the ability of each catalyst to hydrogenate carbonates into formates, a “formates to carbonates intensity ratio” was calculated and followed throughout the first to third cycles of adsorption for the various temperatures (Fig. 9f). Bands at 1535–1533 and 1575–1569 cm^{-1} were chosen as representative frequencies for carbonates and formates, respectively. Comparing the evolution of the ratio by temperature, clear trends could be observed at 500 and 550 K, while at 450 K, the ratio remained roughly constant at ca. 1 throughout cycles, which indicated a poor reduction of carbonates to formates at this temperature. At 500 and 550 K, the ratio was approximately 1.5 and 1.3, respectively, which pointed out the positive effect of temperature in the transformation of carbonates to formates. In all cases, the increase of the ratio originated from the concurrent decrease in the intensity of carbonate and the increase in the intensity of formate. At 500 K, the Zn/Zr sample yielded the highest ratios at the end of each cycle which indicated the crucial role of the ZnO-ZrO₂ interface to form formate from carbonate. Especially outstanding was the increase of the ratio for the Zn/Cu/Zr sample at 500 and 550 K when hydrogen was introduced into the system (increase highlighted with solid black in lines in Fig. 9f). This behavior revealed the good ability of the Zn/Cu/Zr configuration in the hydrogenation of carbonate to formate. In addition, the Zn/Cu/Zr was the unique sample that exhibited a rising ratio during H₂ flow under any condition. This indicated that the Zn/Cu/Zr configuration was able to remain active in the transformation of carbonate to formate during the 10 min of H₂ flow, presumably due to a greater ability to keep CO₂ adsorbed, as observed in Fig. 8.

3.6. Catalytic performance evaluation

The catalytic performance of Cu-Zn on zirconia catalysts is illustrated in Fig. 10 for the three selected reaction temperatures: 450, 500 and 550 K. Fig. 10a shows the CO₂ conversion, Fig. 10b–c show the production of CH₃OH expressed as the space-time yield in $\text{mmol}_{\text{CH}_3\text{OH}} \text{g}_{\text{cat}}^{-1} \text{h}^{-1}$ and in $\text{mmol}_{\text{CH}_3\text{OH}} \text{g}_{\text{Cu}}^{-1} \text{h}^{-1}$, respectively, and Fig. 10d shows the product selectivity for CH₃OH, CO and CH₄. Among the three reaction temperatures tested, all the catalysts showed activity at 500 and 550 K, while there was no measurable activity at 450 K. Greater CO₂ conversion values were achieved for all the samples with increasing reaction temperature. The CO₂ conversion values attained with both Cu- and Zn-containing samples, i.e., Zn/Cu/Zn/Zr, Zn/Cu/Zr and Cu/Zn/Zr, were higher than those achieved with Zn/Zr, Cu/Zr and Zr samples, which evidenced the importance of the Cu-Zn interactions in the CO₂ hydrogenation reaction in accordance with the literature [18,19,87]. Interestingly, the addition of Zn on top of Cu (Zn/Cu/Zr and Zn/Cu/Zn/Zr samples) promoted CO₂ conversion, and the most remarkable improvement occurred at 550 K, with conversion values of approximately 9% for Zn/Cu/ZrO₂ and 6.5% for Zn/Cu/Zn/ZrO₂. Under the same operating conditions, the other samples (Cu/Zn/Zr, Cu/Zr and Zn/Zr) yielded CO₂ conversion values between 2% and 4%.

Regarding the product selectivity (Fig. 10d), temperature had a remarkable effect on the product distribution. At 500 K, the prevailing product was methanol with all catalyst combinations (except on the Zr sample, which only produced CO). Thus, the highest CH₃OH selectivity was achieved at 500 K with Zn/Cu/Zn/Zr sample (close to 80%) followed by Zn/Cu/Zr (71%) and Cu/Zn/Zr (68%) samples. The selectivity toward CO increased significantly when increasing the temperature from 500 to 550 K, according to the endothermicity of the reverse-WGS reaction ($\Delta H^\circ_{298\text{K}} = +41 \text{ kJ mol}^{-1}$) [88]. Advantageously, the Zn/Cu/Zr sample did not produce any methane under any of the conditions, in contrast to the Zn/Cu/Zn/Zr and Cu/Zn/Zr samples that produced methane at both 500 and 550 K with selectivities around 3–6%.

In terms of methanol production (Fig. 10b–c), the most efficient catalysts were Zn/Cu/Zn/Zr and Zn/Cu/Zr, with similar production rates at 500 K ($\sim 1.9 \text{ mmol}_{\text{CH}_3\text{OH}} \text{g}_{\text{cat}}^{-1} \text{h}^{-1}$) and 550 K (\sim

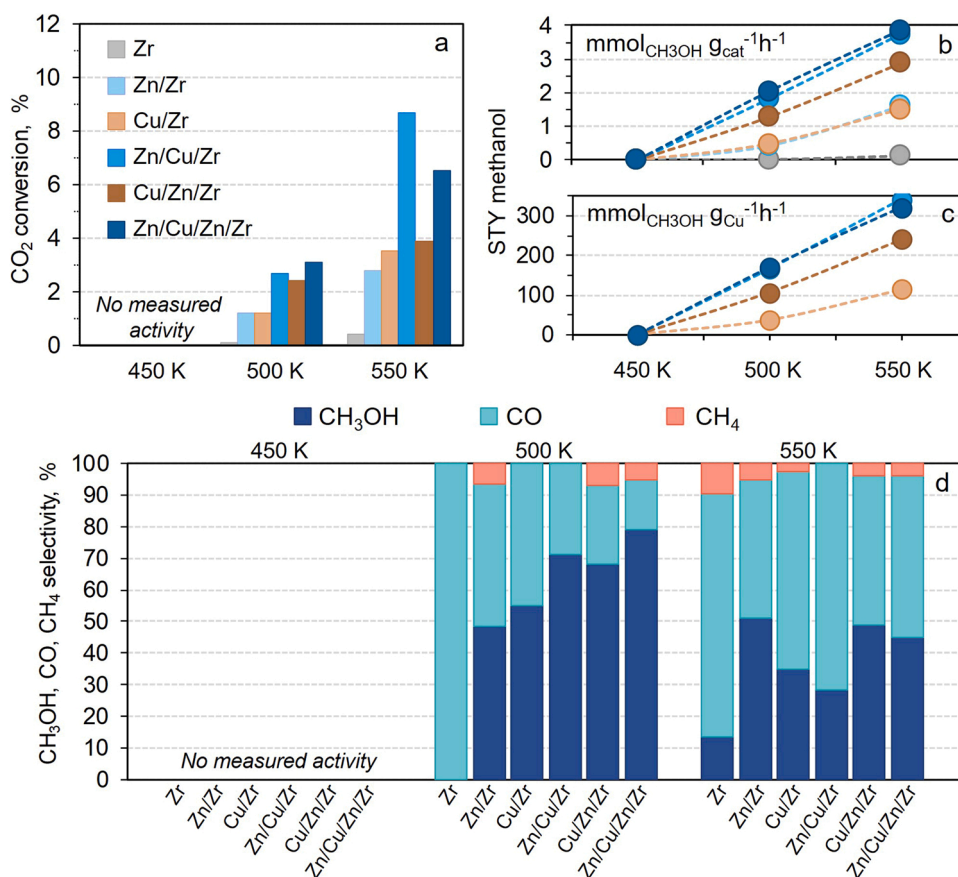


Fig. 10. CO₂ conversion (a), CH₃OH space-time yield in mmol_{CH₃OH} g_{cat}⁻¹ h⁻¹ (b), CH₃OH space-time yield in mmol_{CH₃OH} g_{Cu}⁻¹ h⁻¹ (c), and CH₃OH, CO and CH₄ selectivity (d) for each catalyst. Experimental conditions: 3.0 MPa; 450, 500 and 550 K; reaction mixture composed of H₂/CO₂/N₂ (71/23/6, v/v/v); gas hourly space velocity (GHSV) of 7500 h⁻¹. The data were collected after 90 min under the given operating conditions.

3.8 mmol_{CH₃OH} g_{cat}⁻¹ h⁻¹). For Cu/Zn/Zr sample, the methanol production was lower (1.3 and 2.9 mmol_{CH₃OH} g_{cat}⁻¹ h⁻¹ at 500 and 550 K, respectively). Moreover, Zn/Cu/Zr and Zn/Cu/Zn/Zr samples showed a space-time yield of methanol approximately three times higher than that achieved with Cu/Zr and Zn/Zr samples. When the methanol production was referred to in terms of grams of copper (Fig. 10c), the Zn/Cu/Zr sample produced 165 and 340 mmol_{CH₃OH} g_{Cu}⁻¹ h⁻¹ at 500 and 550 K (similar rates were attained with the Zn/Cu/Zn/Zr sample), while the Cu/Zn/Zr sample produced 107 and 241 mmol_{CH₃OH} g_{Cu}⁻¹ h⁻¹ under the same operating conditions. Therefore, the activity results highlight the potential interest of adding Zn by atomic layer deposition after Cu to promote methanol production catalysis.

3.7. On the impact of zinc promoter produced by ALD on carbon dioxide hydrogenation to methanol

The presence of zinc oxide overlayers on top of copper particles in industrial-type Cu/ZnO/Al₂O₃ catalysts during the hydrogenation of carbon oxides to methanol has been demonstrated in diverse studies during the last decade [11,89,90]. Schott *et al.* [91] reported the unique properties of ZnO layers on the surface of copper particles due to the partial reduction of ZnO to a less strongly oxidized Zn^{δ+} state under the reducing conditions of methanol synthesis. Similarly, Behrens and collaborators [11] demonstrated that the Cu-ZnO synergy lies in their strong metal support interaction leading to partial coverage of the copper surface with ZnO_x under reducing (activation) conditions. Thus, ZnO nanoparticles dispersed on top of copper are special entities that could show particular physico-chemical properties not observed for bulk oxides [38,89,92].

As previously described in the introduction there seems to be agreement among scholars in setting the optimal coverage of copper particles by ZnO_x for a higher catalytic activity at relatively low values of 15–20% monolayer (ML) [19,38,40]. Nevertheless, higher coverages (θ_{Zn} = 0.47) have also been reported as optimal values [41]. Although this difference is not fully understood, all of these studies agree that larger coverages of ZnO may negatively affect the catalyst activity in terms of methanol production [19,38,40,41]. Furthermore, the computational studies carried out by Kuld and coworkers [41] predicted a greater TOF of methanol for ZnO particles smaller than 7 nm, sizes that can be easily accomplished by ALD. Based on our results, we observed that zinc added by one ALD cycle yielded ~15% ML of ZnO, while we speculate that Cu formed larger structures from nanoparticles to small clusters. Based on this remark, the addition of copper by impregnation after zinc ALD might have disabled some of the ZnO species and prevented their assistance in any further reaction. This speculation is supported by the similar methanol production rates observed for Zn/Cu/Zr and Zn/Cu/Zn/Zr samples.

To place these arguments and calculations on a more solid basis, we have compared the results included in this manuscript with the results reported in the literature for earlier studies (Table 4). In our work, with the Zn/Cu/Zr sample, we report rates of 165 and 340 mmol_{CH₃OH} g_{Cu}⁻¹ h⁻¹ at 500 and 550 K, respectively, while 169 and 321 mmol_{CH₃OH} g_{Cu}⁻¹ h⁻¹ were produced with the Zn/Cu/Zn/Zr sample under the same temperature conditions. Recently, Saedy *et al.* [48] accomplished a methanol productivity of ~56 mmol_{CH₃OH} g_{Cu}⁻¹ h⁻¹ at 523 K and 3.0 MPa with a ZnO/Cu/Al₂O₃ catalyst (Zn added by PCVD) and a Zn/Cu atomic ratio of 0.5. Higher Zn/Cu atomic ratios (up to 1.64) did not significantly affect the production of methanol. It is also important

Table 4

Summary table comparing the areal number density (Zn atoms nm⁻²), % monolayer of ZnO, experimental conditions (pressure and temperature), CO₂ conversion, methanol selectivity and space-time yield of methanol (mmol_{CH₃OH} g_{Cu}⁻¹h⁻¹) of the Zn-Cu-containing samples presented in this work and other literature values for similar studies. A H₂/CO₂ molar ratio of approximately 3 was used in all the studies reported in this table.

Catalyst	Synthesis method	Areal number density, Zn atoms nm ⁻²	% of monolayer (ML) of ZnO	P, MPa	T, K	X _{CO₂} , %	S _{CH₃OH} , %	STY, mmol _{CH₃OH} g _{Cu} ⁻¹ h ⁻¹	Ref.
Zn/Zr sample	ALD	1.9	16%	3.0	500	1.2%	48.5%	n.a.	Present work
Cu/Zr sample	IWI	n.a.	n.a.	3.0	500	2.8%	51%	37	Present work
Cu/Zn/Zr sample	ALD	1.6	14%	3.0	500	3.5%	35%	115	Present work
Zn/Cu/Zr sample	ALD	1.5	13%	3.0	500	2.4%	68%	107	Present work
Zn/Cu/Zn/Zr sample	ALD	3.1	27%	3.0	550	3.9%	49%	241	Present work
ZnO/Cu/Al ₂ O ₃	PCVD (zinc deposition time, 2 h)	~1.2	~10%	3.0	500	2.7%	71%	165	Present work
ZnO/Cu/Al ₂ O ₃	PCVD (zinc deposition time, 9 h)	~4.4	~37%	3.0	550	8.7%	28.5%	340	Present work
ZnO/Cu/SiO ₂	ALD	~0.6	~5%	3.0	500	3.1%	79%	169	Present work
					550	6.5%	45%	321	Saedy et al. [48]
					523	ca. 1.2%	ca. 65%	56	Saedy et al. [48]
					523	ca. 1.3%	ca. 60%	ca. 55	Gao et al. [27]
				4.0	523	–	10.1%	10.6	

to highlight that we achieved a similar areal number density and % of ML of ZnO for the Zn/Cu/Zr sample to those reported by Saedy et al. (~1.5 Zn atoms/nm², ~13% ML). In a similar study, Gao et al. [27] synthesized ALD ZnO-coated Cu/SiO₂ catalysts with various exposure times and ALD cycles and tested them in the hydrogenation of carbon dioxide. Among the prepared catalysts, the most active catalyst (exposure time of 30 s to the Zn precursor and one ALD cycle) was more selective toward carbon monoxide (96 mmol_{CO} g_{Cu}⁻¹h⁻¹) than toward methanol (10.6 mmol_{CH₃OH} g_{Cu}⁻¹h⁻¹) at 523 K and 4.0 MPa. However, for that particular ZnO/Cu/SiO₂ catalyst, the areal number density was significantly lower than the value that we report in our manuscript (~0.6 Zn atoms/nm², ~5% ML).

In general, the data included in Table 4 highlight the good performance of the catalysts prepared and tested in the present work for carbon dioxide hydrogenation to methanol. It is worth mentioning that this level of activity was achieved with relatively low Cu and Zn metal loadings (~1–2 wt%) which led to considerably high methanol production rates when they were expressed per gram of copper. This range of metal contents seemed to be relatively efficient to achieve a good and even distribution of both copper and zinc and to produce a significant amount of active ZnO-Cu sites. As a future challenge, it would be worth investigating whether it is viable to obtain similar methanol production rates per gram of copper with higher metal contents. In this context, atomic layer deposition (ALD) can be an outstanding synthesis method for the scale up of catalysts toward higher metal loadings.

4. Conclusions

Tuning the interaction of zinc and copper must be considered an important parameter to control the catalytic performance toward methanol formation. In this work, by alternating the order in which metal (copper) and promoter (zinc) were added to the catalyst, a series of catalysts with various metal-promoter-support configurations were synthesized. The order in which the zinc promoter was introduced onto the catalyst by atomic layer deposition (ALD) compared to the active copper metal by impregnation affected the catalytic activity. Zinc ALD after copper impregnation (zinc-on-copper) yielded higher CO₂ conversion and methanol production rates than copper-on-zinc, although the overall copper and zinc loadings were similar. Advantageously, unlike the other catalysts, the zinc-on-copper zirconia catalyst (Zn/Cu/Zr sample) did not produce any methane with high methanol production rates under the tested operating conditions.

Infrared studies of cyclic adsorption of CO₂ and H₂ revealed that zinc ALD on impregnated copper accumulated carbonates and bicarbonates (CO₃²⁻, HCO₃⁻) exceptionally well during the carbon dioxide feed and

transformed them into formate species (*HCOO) during the hydrogen feed. Together with the higher CO₂ conversion and methanol production rate achieved with the Zn/Cu/Zr sample, this suggests that the catalytic activity to some extent relies on the ability of the catalyst to transform carbonates to formates. The DFT calculations accurately predicted the band position for formate species on different model surfaces (i.e., ZnO/ZrO₂, Cu(111) and Cu(110)) compared to the experimental bands observed by DRIFTS. The formate pathway was the favored mechanistic route of carbon dioxide hydrogenation to methanol under the selected experimental conditions. In addition, the CO₂ temperature programmed desorption analyses showed the great capacity of the zinc-copper on zirconia catalyst for the adsorption of CO₂. When evaluating the molecules of CO₂ adsorbed per atom of zinc, the zinc-on-copper configuration adsorbed more CO₂ molecules than the copper-on-zinc configuration (0.67 versus 0.45 molecules CO₂ per zinc atom). Additionally, according to TPR studies, the zinc deposited after copper impregnation improved the homogeneity of copper oxide species and the reducibility of the bulk CuO.

Overall, this work provides insight into the significance of the zinc oxide/copper/zirconia interactions for selective hydrogenation of carbon dioxide to methanol and highlights the potential of atomic layer deposition (ALD) in the synthesis of atomically dispersed metal catalysts for an efficient methanol synthesis.

CRedit authorship contribution statement

Aitor Arandia: Conceptualization, Investigation, Methodology, Formal analysis, Validation, Visualization, Supervision, Writing – original draft, Writing – review & editing. **Jihong Yim:** Investigation, Methodology, Formal analysis, Validation, Writing – review & editing. **Hassaan Warraich:** Investigation, Formal analysis, Methodology. **Emilia Leppäkangas:** Investigation, Methodology. **René Bes:** Investigation, Formal analysis, Writing – review & editing. **Aku Lempelto:** Investigation, Software, Formal analysis, Visualization, Writing – review & editing. **Lars Gell:** Investigation, Software, Formal analysis, Visualization, Writing – review & editing. **Hua Jiang:** Investigation. **Kristoffer Meinander:** Investigation, Formal analysis, Visualization, Writing – review & editing. **Tiia Viinikainen:** Methodology, Writing – review & editing. **Karoliina Honkala:** Conceptualization, Writing – review & editing, Funding acquisition. **Simo Huotari:** Investigation, Formal analysis, Visualization, Writing – review & editing. **Riikka L. Puurunen:** Conceptualization, Methodology, Resources, Writing – review & editing, Supervision, Project administration, Funding acquisition.

Declaration of Competing Interest

The authors declare that they have no known competing financial interests or personal relationships that could have appeared to influence the work reported in this paper.

Data Availability

Data will be made available on request.

Acknowledgements

The work at Aalto University has been financially supported by the Academy of Finland (COOLCAT consortium, decision no. 329977 and 329978; ALDI consortium, decision no. 331082). This work made use of Aalto University Bioeconomy, OtaNano and RawMatters infrastructure. Hannu Revitzer (Aalto University) is thanked for the ICP-OES analysis, Aalto workshop people (especially Seppo Jääskeläinen) for working on the reactor modifications. The DFT calculations were made possible by computational resources provided by the CSC — IT Center for Science, Espoo, Finland (<https://www.csc.fi/en/>) and computer capacity from the Finnish Grid and Cloud Infrastructure (urn:nbn:fi:research-infras-2016072533). The University of Helsinki acknowledges support from Academy of Finland (project 295696) as well as ESRF for beamtime and Blanka Detlefs and Christoph Sahle for expert support. Preliminary XANES measurements were performed using the Helsinki Center for X-ray Spectroscopy Hel-XAS instrument under the proposal number 2021–0011.

Appendix A. Supporting information

Supplementary data associated with this article can be found in the online version at [doi:10.1016/j.apcatb.2022.122046](https://doi.org/10.1016/j.apcatb.2022.122046).

References

- [1] T.A. Atspha, T. Yoon, P. Seongho, C.J. Lee, A review on the catalytic conversion of CO₂ using H₂ for synthesis of CO, methanol, and hydrocarbons, *J. CO₂ Util.* 44 (2021), 101413, <https://doi.org/10.1016/j.jcou.2020.101413>.
- [2] J. Zhong, X. Yang, Z. Wu, B. Liang, Y. Huang, T. Zhang, State of the art and perspectives in heterogeneous catalysis of CO₂ hydrogenation to methanol, *Chem. Soc. Rev.* 49 (2020) 1385–1413, <https://doi.org/10.1039/c9cs00614a>.
- [3] S. Roy, A. Cherevotan, S.C. Peter, Thermochemical CO₂ hydrogenation to single carbon products: scientific and technological challenges, *ACS Energy Lett.* 3 (2018) 1938–1966, <https://doi.org/10.1021/acsenenergylett.8b00740>.
- [4] J. Andersson, A. Krüger, S. Grönkvist, Methanol as a carrier of hydrogen and carbon in fossil-free production of direct reduced iron, *Energy Convers. Manag.* X. 7 (2020), 100051, <https://doi.org/10.1016/j.ecmx.2020.100051>.
- [5] O.Y.H. Elseragawy, A. Hoadley, J. Patel, T. Bhatelia, S. Lim, N. Haque, C. Li, Thermo-economic analysis of reverse water-gas shift process with different temperatures for green methanol production as a hydrogen carrier, *J. CO₂ Util.* 41 (2020) 101280–101289, <https://doi.org/10.1016/j.jcou.2020.101280>.
- [6] S.S. Araya, V. Liso, X. Cui, N. Li, J. Zhu, S.L. Sahlin, S.H. Jensen, M.P. Nielsen, S. K. Kær, A review of the methanol economy: the fuel cell route, *Energies* 13 (2020) 596–627, <https://doi.org/10.3390/en13030596>.
- [7] S. Verhelst, J.W. Turner, L. Sileghem, J. Vancoillie, Methanol as a fuel for internal combustion engines, *Prog. Energy Combust. Sci.* 70 (2019) 43–88, <https://doi.org/10.1016/j.pecs.2018.10.001>.
- [8] T. Li, T. Shoinchorova, J. Gascon, J. Ruiz-Martinez, Aromatics production via methanol-mediated transformation routes, *ACS Catal.* 11 (2021) 7780–7819, <https://doi.org/10.1021/acscatal.1c01422>.
- [9] S. Ren, X. Fan, Z. Shang, W.R. Shoemaker, L. Ma, T. Wu, S. Li, N.B. Klinghoffer, M. Yu, X. Liang, Enhanced catalytic performance of Zr modified CuO/ZnO/Al₂O₃ catalyst for methanol and DME synthesis via CO₂ hydrogenation, *J. CO₂ Util.* 36 (2020) 82–95, <https://doi.org/10.1016/j.jcou.2019.11.013>.
- [10] I. Abbas, H. Kim, C.H. Shin, S. Yoon, K.D. Jung, Differences in bifunctionality of ZnO and ZnO₂ in Cu/ZnO/ZrO₂/Al₂O₃ catalysts in hydrogenation of carbon oxides for methanol synthesis, *Appl. Catal. B Environ.* 258 (2019) 117971–117981, <https://doi.org/10.1016/j.apcatb.2019.117971>.
- [11] M. Behrens, F. Studt, I. Kasatkin, S. Kühl, M. Hävecker, F. Abild-pedersen, S. Zander, F. Girgsdies, P. Kurr, B.-L. Kniep, M. Tovar, R.W. Fischer, J.K. Nørskov, R. Schlögl, The Active Site of Methanol Synthesis over Cu/ZnO/Al₂O₃ Industrial Catalysts, *Science* 336 (2012) 893–897, <https://doi.org/10.1126/science.1219831>.
- [12] L.C. Grabow, M. Mavrikakis, Mechanism of methanol synthesis on Cu through CO₂ and CO hydrogenation, *ACS Catal.* 1 (2011) 365–384, <https://doi.org/10.1021/cs200055d>.
- [13] S.G. Jadhav, P.D. Vaidya, B.M. Bhanage, J.B. Joshi, Catalytic carbon dioxide hydrogenation to methanol: a review of recent studies, *Chem. Eng. Res. Des.* 92 (2014) 2557–2567, <https://doi.org/10.1016/j.cherd.2014.03.005>.
- [14] G.C. Chinchin, P.J. Denny, D.G. Parker, M.S. Spencer, D.A. Whan, Mechanism of methanol synthesis from CO₂/CO/H₂ mixtures over copper/zinc oxide/alumina catalysts: use of ¹⁴C-labelled reactants, *Appl. Catal.* 30 (1987) 333–338, [https://doi.org/10.1016/S0166-9834\(00\)84123-8](https://doi.org/10.1016/S0166-9834(00)84123-8).
- [15] J. Zhu, Y. Su, J. Chai, V. Muravev, N. Kosinov, E.J.M. Hensen, Mechanism and nature of active sites for methanol synthesis from CO/CO₂ on Cu/CeO₂, *ACS Catal.* 10 (2020) 11532–11544, <https://doi.org/10.1021/acscatal.0c02909>.
- [16] J. Skrzypek, M. Lachowska, H. Moroz, Kinetics of methanol synthesis over commercial copper/zinc oxide/alumina catalysts, *Chem. Eng. Sci.* 46 (1991) 2809–2813, [https://doi.org/10.1016/0009-2509\(91\)85150-V](https://doi.org/10.1016/0009-2509(91)85150-V).
- [17] U.J. Etim, Y. Song, Z. Zhong, Improving the Cu/ZnO-based catalysts for carbon dioxide hydrogenation to methanol, and the use of methanol as a renewable energy storage media, *Front. Earth Sci.* 8 (2020) 1–26, <https://doi.org/10.3389/feart.2020.545431>.
- [18] Y. Wang, S. Kattel, W. Gao, K. Li, P. Liu, J.G. Chen, H. Wang, Exploring the ternary interactions in Cu–ZnO–ZrO₂ catalysts for efficient CO₂ hydrogenation to methanol, *Nat. Commun.* 10 (2019) 1166, <https://doi.org/10.1038/s41467-019-09072-6>.
- [19] S. Kattel, P.J. Ramírez, J.G. Chen, J.A. Rodríguez, P. Liu, Active sites for CO₂ hydrogenation to methanol on Cu/ZnO catalysts, *Science* 355 (2017) 1296–1299, <https://doi.org/10.1126/science.aal3573>.
- [20] D. Laudenschlager, H. Ruland, M. Muhler, Identifying the nature of the active sites in methanol synthesis over Cu/ZnO/Al₂O₃ catalysts, *Nat. Commun.* 11 (2020) 3898, <https://doi.org/10.1038/s41467-020-17631-5>.
- [21] Y. Lu, Z. Zhang, H. Wang, Y. Wang, Toward efficient single-atom catalysts for renewable fuels and chemicals production from biomass and CO₂, *Appl. Catal. B Environ.* 292 (2021) 120162–120199, <https://doi.org/10.1016/j.apcatb.2021.120162>.
- [22] A.O. Elnabawy, J. Schumann, P. Bothra, A. Cao, J.K. Nørskov, The Challenge of CO₂ hydrogenation to methanol: fundamental limitations imposed by linear scaling relations, *Top. Catal.* 63 (2020) 635–648, <https://doi.org/10.1007/s11244-020-01283-2>.
- [23] B. Hu, Y. Yin, G. Liu, S. Chen, X. Hong, S.C.E. Tsang, Hydrogen spillover enabled active Cu sites for methanol synthesis from CO₂ hydrogenation over Pd doped CuZn catalysts, *J. Catal.* 359 (2018) 17–26, <https://doi.org/10.1016/j.jcat.2017.12.029>.
- [24] J. Toyir, P.R. De la Piscina, J.L.G. Fierro, N. Homs, Catalytic performance for CO₂ conversion to methanol of gallium-promoted copper-based catalysts: influence of metallic precursors, *Appl. Catal. B Environ.* 34 (2001) 255–266, [https://doi.org/10.1016/S0926-3373\(01\)00203-X](https://doi.org/10.1016/S0926-3373(01)00203-X).
- [25] L. Martínez-Suarez, N. Siemer, J. Frenzel, D. Marx, Reaction network of methanol synthesis over Cu/ZnO nanocatalysts, *ACS Catal.* 5 (2015) 4201–4218, <https://doi.org/10.1021/acscatal.5b00442>.
- [26] Y. Sun, C. Huang, L. Chen, Y. Zhang, M. Fu, J. Wu, D. Ye, Active site structure study of Cu/Plate ZnO model catalysts for CO₂ hydrogenation to methanol under the real reaction conditions, *J. CO₂ Util.* 37 (2020) 55–64, <https://doi.org/10.1016/j.jcou.2019.11.029>.
- [27] J. Gao, P.E. Boahene, Y. Hu, A. Dalai, H. Wang, Atomic layer deposition ZnO over-coated Cu/SiO₂ catalysts for methanol synthesis from CO₂ hydrogenation, *Catalysts* 9 (2019) 922–938, <https://doi.org/10.3390/catal9110922>.
- [28] T. Witton, J. Chalorngtham, P. Dumrongbunditkul, M. Chareonpanich, J. Limtrakul, CO₂ hydrogenation to methanol over Cu/ZrO₂ catalysts: Effects of zirconia phases, *Chem. Eng. J.* 293 (2016) 327–336, <https://doi.org/10.1016/j.cej.2016.02.069>.
- [29] K. Li, J.G. Chen, CO₂ hydrogenation to methanol over ZrO₂-containing catalysts: insights into ZrO₂ induced synergy, *ACS Catal.* 9 (2019) 7840–7861, <https://doi.org/10.1021/acscatal.9b01943>.
- [30] X. Jiang, X. Nie, X. Guo, C. Song, J.G. Chen, Recent advances in carbon dioxide hydrogenation to methanol via heterogeneous catalysis, *Chem. Rev.* 120 (2020) 7984–8034, <https://doi.org/10.1021/acs.chemrev.9b00723>.
- [31] F. Arena, K. Barbera, G. Italiano, G. Bonura, L. Spadaro, F. Frusteri, Synthesis, characterization and activity pattern of Cu–ZnO/ZrO₂ catalysts in the hydrogenation of carbon dioxide to methanol, *J. Catal.* 249 (2007) 185–194, <https://doi.org/10.1016/j.jcat.2007.04.003>.
- [32] S. Velu, K. Suzuki, C.S. Gopinath, H. Yoshida, T. Hattori, XPS, XANES and EXAFS investigations of CuO/ZnO/Al₂O₃/ZrO₂ mixed oxide catalysts, *Phys. Chem. Chem. Phys.* 4 (2002) 1990–1999, <https://doi.org/10.1039/b109766k>.
- [33] W. Wang, Z. Qu, L. Song, Q. Fu, CO₂ hydrogenation to methanol over Cu/CeO₂ and Cu/ZrO₂ catalysts: Tuning methanol selectivity via metal-support interaction, *J. Energy Chem.* 40 (2020) 22–30, <https://doi.org/10.1016/j.jechem.2019.03.001>.
- [34] J. Wang, G. Li, Z. Li, C. Tang, Z. Feng, H. An, H. Liu, T. Liu, C. Li, A highly selective and stable ZnO–ZrO₂ solid solution catalyst for CO₂ hydrogenation to methanol, *Sci. Adv.* 3 (2017) 1–11, <https://doi.org/10.1126/sciadv.1701290>.
- [35] Z. Han, C. Tang, F. Sha, S. Tang, J. Wang, C. Li, CO₂ hydrogenation to methanol on ZnO–ZrO₂ solid solution catalysts with ordered mesoporous structure, *J. Catal.* 396 (2021) 242–250, <https://doi.org/10.1016/j.jcat.2021.02.024>.
- [36] N. Rui, R. Shi, R.A. Gutiérrez, R. Rosales, J. Kang, M. Mahapatra, P.J. Ramírez, S. D. Senanayake, J.A. Rodríguez, CO₂ hydrogenation on ZrO₂/Cu(111) surfaces: production of methane and methanol, *Ind. Eng. Chem. Res.* 60 (2021) 18900–18906, <https://doi.org/10.1021/acs.iecr.1c03229>.

- [37] C. Wu, L. Lin, J. Liu, J. Zhang, F. Zhang, T. Zhou, N. Rui, S. Yao, Y. Deng, F. Yang, W. Xu, J. Luo, Y. Zhao, B. Yan, X.D. Wen, J.A. Rodriguez, D. Ma, Inverse ZrO_2/Cu as a highly efficient methanol synthesis catalyst from CO_2 hydrogenation, *Nat. Commun.* 11 (2020) 5767–5776, <https://doi.org/10.1038/s41467-020-19634-8>.
- [38] R.M. Palomino, P.J. Ramirez, Z. Liu, R. Hamlyn, I. Waluyo, M. Mahapatra, I. Orozco, A. Hunt, J.P. Simonovis, S.D. Senanayake, J.A. Rodriguez, Hydrogenation of CO_2 on $\text{ZnO}/\text{Cu}(100)$ and $\text{ZnO}/\text{Cu}(111)$ catalysts: role of copper structure and metal-oxide interface in methanol synthesis, *J. Phys. Chem. B* 122 (2018) 794–800, <https://doi.org/10.1021/acs.jpcc.7b06901>.
- [39] F. Liao, Y. Huang, J. Ge, W. Zheng, K. Tedsree, P. Collier, X. Hong, S.C. Tsang, Morphology-dependent interactions of ZnO with Cu nanoparticles at the materials' interface in selective hydrogenation of CO_2 to CH_3OH , *Angew. Chem. Int. Ed.* 50 (2011) 2162–2165, <https://doi.org/10.1002/anie.201007108>.
- [40] J. Nakamura, I. Nakamura, T. Uchijima, T. Watanabe, T. Fujitani, Model studies of methanol synthesis on copper catalysts, *Stud. Surf. Sci. Catal.* 101 B (1996) 1389–1399, [https://doi.org/10.1016/s0167-2991\(96\)80351-x](https://doi.org/10.1016/s0167-2991(96)80351-x).
- [41] S. Kuld, M. Thorhauge, H. Falsig, C.F. Elkjær, S. Helveg, I. Chorkendorff, J. Sehested, Quantifying the promotion of Cu catalysts by ZnO for methanol synthesis, *Sci. (80-.)* 352 (2016) 969–974, <https://doi.org/10.1126/science.aaf0718>.
- [42] J.R. van Ommen, A. Goulas, R.L. Puurunen, Atomic layer deposition, *kirk-othmer encycl., Chem. Technol.* (2021) 1–42, <https://doi.org/10.1002/0471238961.koe00059>.
- [43] B. Zhang, Y. Qin, Interface tailoring of heterogeneous catalysts by atomic layer deposition, *ACS Catal.* 8 (2018) 10064–10081, <https://doi.org/10.1021/acscatal.8b02659>.
- [44] B.J. Oneill, D.H.K. Jackson, J. Lee, C. Canlas, P.C. Stair, C.L. Marshall, J.W. Elam, T.F. Kuech, J.A. Dumesic, G.W. Huber, Catalyst design with atomic layer deposition, *ACS Catal.* 5 (2015) 1804–1825, <https://doi.org/10.1021/cs501862h>.
- [45] J.A. Singh, N. Yang, S.F. Bent, Nanoengineering heterogeneous catalysts by atomic layer deposition, *Annu. Rev. Chem. Biomol. Eng.* 8 (2017) 41–62, <https://doi.org/10.1146/annurev-chembioeng-060816-101547>.
- [46] I. Ro, Y. Liu, M.R. Ball, D.H.K. Jackson, J.P. Chada, C. Sener, T.F. Kuech, R. J. Madon, G.W. Huber, J.A. Dumesic, Role of the Cu-ZrO_2 interfacial sites for conversion of ethanol to ethyl acetate and synthesis of methanol from CO_2 and H_2 , *ACS Catal.* 6 (2016) 7040–7050, <https://doi.org/10.1021/acscatal.6b01805>.
- [47] F. Zhao, M. Gong, K. Cao, Y. Zhang, J. Li, R. Chen, Atomic layer deposition of Ni on Cu nanoparticles for methanol synthesis from CO_2 hydrogenation, *ChemCatChem* 9 (2017) 3772–3778, <https://doi.org/10.1002/cctc.201700622>.
- [48] S. Saedy, M.A. Newton, M. Zabilskiy, J.H. Lee, F. Krumeich, M. Ranocchiari, J. van Bokhoven, Copper-zinc oxide interface as a methanol-selective structure in Cu-ZnO catalyst during catalytic hydrogenation of carbon dioxide to methanol, *Catal. Sci. Technol.* 12 (2022) 2703–2716, <https://doi.org/10.1039/d2cy00224h>.
- [49] X. Liu, J. Luo, H. Wang, L. Huang, S. Wang, S. Li, Z. Sun, F. Sun, Z. Jiang, S. Wei, W. X. Li, J. Lu, In situ spectroscopic characterization and theoretical calculations identify partially reduced $\text{ZnO}1-x/\text{Cu}$ interfaces for methanol synthesis from CO_2 , *Angew. Chem. Int. Ed.* 61 (2022), <https://doi.org/10.1002/anie.202202330>.
- [50] S. Brunauer, P.H. Emmett, E. Teller, Adsorption of gases in multimolecular layers, *J. Am. Chem. Soc.* 60 (1938) 309–319, <https://doi.org/10.1021/ja01269a023>.
- [51] P.P. Halenda, E.P. Barrett, L.G. Joyner, The determination of pore volume and area distributions in porous substances. I. Computations from nitrogen isotherms, *J. Am. Chem. Soc.* 73 (1951) 373–380, <https://doi.org/10.1021/ja01145a126>.
- [52] S. Huotari, C.J. Sahle, C. Henriquet, A. Al-Zein, K. Martel, L. Simonelli, R. Verbeni, H. Gonzalez, M.C. Lagier, C. Ponchut, M. Moretti Sala, M. Krish, G. Monaco, A large-solid-angle X-ray Raman scattering spectrometer at ID20 of the European Synchrotron Radiation Facility, *J. Synchrotron Radiat.* 24 (2017) 521–530, <https://doi.org/10.1107/S1600577516020579>.
- [53] M.M. Sala, K. Martel, C. Henriquet, A. Al Zein, L. Simonelli, C.J. Sahle, H. Gonzalez, M.C. Lagier, C. Ponchut, S. Huotari, R. Verbeni, M. Krish, G. Monaco, A high-energy-resolution resonant inelastic X-ray scattering spectrometer at ID20 of the European Synchrotron Radiation Facility, *J. Synchrotron Radiat.* 25 (2018) 580–591, <https://doi.org/10.1107/S1600577518001200>.
- [54] J. Wellendorff, K.T. Lundgaard, A. Møgelhøj, V. Petzold, D.D. Landis, J.K. Nørskov, T. Bligaard, K.W. Jacobsen, Density functionals for surface science: Exchange-correlation model development with Bayesian error estimation, *Phys. Rev. B* 85 (2012) 32–34, <https://doi.org/10.1103/PhysRevB.85.235149>.
- [55] J. Enkovaara, C. Rostgaard, J.J. Mortensen, J. Chen, M. Dulak, L. Ferrighi, J. Gavnholdt, C. Glinsvad, V. Haikola, H.A. Hansen, H.H. Kristoffersen, M. Kuisma, A.H. Larsen, L. Lehtovaara, M. Ljungberg, O. Lopez-Acevedo, P.G. Moses, J. Ojanen, T. Olsen, V. Petzold, N.A. Romero, J. Stausholm-Møller, M. Strange, G. A. Tritsarlis, M. Vanin, M. Walter, B. Hammer, H. Häkkinen, G.K.H. Madsen, R. M. Nieminen, J.K. Nørskov, M. Puska, T.T. Rantala, J. Schiøtz, K.S. Thygesen, K. W. Jacobsen, Electronic structure calculations with GPAW: A real-space implementation of the projector augmented-wave method, *J. Phys. Condens. Matter* 22 (2010) 253303–253325, <https://doi.org/10.1088/0953-8984/22/25/253202>.
- [56] P.E. Blöchl, Projector augmented-wave method, *Phys. Rev. B* 50 (1994) 17953–17979, <https://doi.org/10.1103/PhysRevB.50.17953>.
- [57] S. Dudarev, G. Botton, Electron-energy-loss spectra and the structural stability of nickel oxide: An LSDA+U study, *Phys. Rev. B - Condens. Matter Mater. Phys.* 57 (1998) 1505–1509, <https://doi.org/10.1103/PhysRevB.57.1505>.
- [58] E. Bitzek, P. Koskinen, F. Gähler, M. Moseler, P. Gumbsch, Structural relaxation made simple, *Phys. Rev. Lett.* 97 (2006) 1–4, <https://doi.org/10.1103/PhysRevLett.97.170201>.
- [59] A. Hjorth Larsen, J. Jørgen Mortensen, J. Blomqvist, I.E. Castelli, R. Christensen, M. Dulak, J. Friis, M.N. Groves, B. Hammer, C. Hargus, E.D. Hermes, P.C. Jennings, P. Bjerre Jensen, J. Kermode, J.R. Kitchin, E. Leonhard Kolsbjerg, J. Kubal, K. Kaasbjerg, S. Lysgaard, J. Bergmann Maronsson, T. Maxson, T. Olsen, L. Pastewka, A. Peterson, C. Rostgaard, J. Schiøtz, O. Schütt, M. Strange, K. S. Thygesen, T. Vegge, L. Vilhelmsen, M. Walter, Z. Zeng, K.W. Jacobsen, The atomic simulation environment - a python library for working with atoms, *J. Phys. Condens. Matter* 29 (2017) 273002–273032, <https://doi.org/10.1088/1361-648X/aa680e>.
- [60] T. Frederiksen, M. Paulsson, M. Brandbyge, A.P. Jauho, Inelastic transport theory from first principles: methodology and application to nanoscale devices, *Phys. Rev. B - Condens. Matter Mater. Phys.* 75 (2007) 1–22, <https://doi.org/10.1103/PhysRevB.75.205413>.
- [61] R.A. Bair, W.A. Goddard, Ab initio studies of the x-ray absorption edge in copper complexes. I. Atomic Cu^{2+} and Cu(II)Cl_2 , *Phys. Rev. B* 22 (1980) 2767–2776, <https://doi.org/10.1103/PhysRevB.22.2767>.
- [62] G. Döring, C. Sternemann, A. Kaprolat, A. Mattila, K. Hämäläinen, W. Schülke, Shake-up valence excitations in CuO by resonant inelastic x-ray scattering, *Phys. Rev. B - Condens. Matter Mater. Phys.* 70 (2004) 1–15, <https://doi.org/10.1103/PhysRevB.70.085115>.
- [63] M.M.R. Bhuiyan, S.D. Lin, T.C. Hsiao, Effect of calcination on Cu-Zn -loaded hydrotalcite catalysts for C-C bond formation derived from methanol, *Catal. Today* 226 (2014) 150–159, <https://doi.org/10.1016/j.cattod.2013.10.053>.
- [64] A. Dadlani, S. Acharya, O. Trejo, D. Nordlund, M. Peron, J. Razavi, F. Berto, F. B. Prinz, J. Torgersen, Revealing the bonding environment of Zn in ALD Zn(O,S) buffer layers through X-ray absorption spectroscopy, *ACS Appl. Mater. Interfaces* 9 (2017) 39105–39109, <https://doi.org/10.1021/acsami.7b06728>.
- [65] A. Montebelli, C.G. Visconti, G. Groppi, E. Tronconi, S. Kohler, H.J. Venvik, R. Myrstad, Washcoating and chemical testing of a commercial $\text{Cu}/\text{ZnO}/\text{Al}_2\text{O}_3$ catalyst for the methanol synthesis over copper open-cell foams, *Appl. Catal. A Gen.* 481 (2014) 96–103, <https://doi.org/10.1016/j.apcata.2014.05.005>.
- [66] E. Diler, B. Lescop, S. Rioual, G. Nguyen Vien, D. Thierry, B. Rouvellou, Initial formation of corrosion products on pure zinc and MgZn_2 examined by XPS, *Corros. Sci.* 79 (2014) 83–88, <https://doi.org/10.1016/j.corsci.2013.10.029>.
- [67] A.R. Puigdollers, P. Schlexer, S. Tosoni, G. Pacchioni, Increasing oxide reducibility: The role of metal/oxide interfaces in the formation of oxygen vacancies, *ACS Catal.* 7 (2017) 6493–6513, <https://doi.org/10.1021/acscatal.7b01913>.
- [68] D. Eder, R. Kramer, The stoichiometry of hydrogen reduced zirconia and its influence on catalytic activity - part 1: volumetric and conductivity studies, *Phys. Chem. Chem. Phys.* 4 (2002) 795–801, <https://doi.org/10.1039/b109887j>.
- [69] W. Donphai, N. Piriayawate, T. Witoon, P. Jantaratanana, V. Varabuntoonvit, M. Chareonpanich, Effect of magnetic field on CO_2 conversion over $\text{Cu-ZnO}/\text{ZrO}_2$ catalyst in hydrogenation reaction, *J. CO₂ Util.* 16 (2016) 204–211, <https://doi.org/10.1016/j.jcou.2016.07.007>.
- [70] L. Zhao, Y. Zhang, S. Bi, Q. Liu, Metal-organic framework-derived $\text{CeO}_2\text{-ZnO}$ catalysts for $\text{C}_3\text{H}_6\text{-SCR}$ of NO : An in situ DRIFTS study, *RSC Adv.* 9 (2019) 19236–19242, <https://doi.org/10.1039/c9ra03103k>.
- [71] R.X. Zhou, X.Y. Jiang, J.X. Mao, X.M. Zheng, Oxidation of carbon monoxide catalyzed by copper-zirconium composite oxides, *Appl. Catal. A Gen.* 162 (1997) 213–222, [https://doi.org/10.1016/S0926-860X\(97\)00099-9](https://doi.org/10.1016/S0926-860X(97)00099-9).
- [72] G. Águila, F. Gracia, J. Cortés, P. Araya, Effect of copper species and the presence of reaction products on the activity of methane oxidation on supported CuO catalysts, *Appl. Catal. B Environ.* 77 (2008) 325–338, <https://doi.org/10.1016/j.apcatb.2007.08.002>.
- [73] K.V.R. Chary, G.V. Sagar, C.S. Srikanth, V.V. Rao, Characterization and catalytic functionalities of copper oxide catalysts supported on zirconia, *J. Phys. Chem. B* 111 (2007) 543–550, <https://doi.org/10.1021/jp063335x>.
- [74] C.Z. Yao, L.C. Wang, Y.M. Liu, G.S. Wu, Y. Cao, W.L. Dai, H.Y. He, K.N. Fan, Effect of preparation method on the hydrogen production from methanol steam reforming over binary Cu/ZrO_2 catalysts, *Appl. Catal. A Gen.* 297 (2006) 151–158, <https://doi.org/10.1016/j.apcata.2005.09.002>.
- [75] A.G. Sato, D.P. Volanti, D.M. Meira, S. Damyanova, E. Longo, J.M.C. Bueno, Effect of the ZrO_2 phase on the structure and behavior of supported Cu catalysts for ethanol conversion, *J. Catal.* 307 (2013) 1–17, <https://doi.org/10.1016/j.jcat.2013.06.022>.
- [76] Y. Yao, X. Wu, O.Y. Gutiérrez, J. Ji, P. Jin, S. Wang, Y. Xu, Y. Zhao, S. Wang, X. Ma, J.A. Lercher, Roles of Cu^+ and Cu^0 sites in liquid-phase hydrogenation of esters on core-shell $\text{CuZn}@C$ catalysts, *Appl. Catal. B Environ.* 267 (2020) 118698–118708, <https://doi.org/10.1016/j.apcatb.2020.118698>.
- [77] C. Huang, S. Chen, X. Fei, D. Liu, Y. Zhang, Catalytic hydrogenation of CO_2 to methanol: Study of synergistic effect on adsorption properties of CO_2 and H_2 in $\text{CuO}/\text{ZnO}/\text{ZrO}_2$ system, *Catalysts* 5 (2015) 1846–1861, <https://doi.org/10.3390/catal5041846>.
- [78] H. Zhan, X. Shi, B. Tang, G. Wang, B. Ma, W. Liu, The performance of $\text{Cu}/\text{Zn}/\text{Zr}$ catalysts of different $\text{Zr}/(\text{Cu}+\text{Zn})$ ratio for CO_2 hydrogenation to methanol, *Catal. Commun.* 149 (2021) 106264–106268, <https://doi.org/10.1016/j.ccatom.2020.106264>.
- [79] S. Kouva, J. Andersin, K. Honkala, J. Lehtonen, L. Lefferts, J. Kanervo, Water and carbon oxides on monoclinic zirconia: experimental and computational insights, *Phys. Chem. Chem. Phys.* 16 (2014) 20650–20664, <https://doi.org/10.1039/c4cp02742f>.
- [80] S.T. Korhonen, M. Calatayud, A. Outi, I. Krause, Structure and stability of formates and carbonates on monoclinic zirconia: a combined study by density functional theory and infrared spectroscopy, *J. Phys. Chem. C* 112 (2008) 16096–16102, <https://doi.org/10.1021/jp803353v>.
- [81] S.P. Köck, Eva Maria, Michaela Kogler, Thomas Bielz, Bernhard Klötzer, In situ FT-IR spectroscopic study of CO_2 and CO adsorption on Y_2O_3 , ZrO_2 , and yttria-

- stabilized ZrO₂, J. Phys. Chem. C. 117 (2013) 17666–17673, <https://doi.org/10.1021/jp405625x>.
- [82] B. Bachiller-Baeza, I. Rodriguez-Ramos, A. Guerrero-Ruiz, Interaction of carbon dioxide with the surface of zirconia polymorphs, Langmuir 14 (1998) 3556–3564, <https://doi.org/10.1021/la970856q>.
- [83] B. An, J. Zhang, K. Cheng, P. Ji, C. Wang, W. Lin, Confinement of ultrasmall Cu/ZnOx nanoparticles in metal-organic frameworks for selective methanol synthesis from catalytic hydrogenation of CO₂, J. Am. Chem. Soc. 139 (2017) 3834–3840, <https://doi.org/10.1021/jacs.7b00058>.
- [84] X. Dong, F. Li, N. Zhao, F. Xiao, J. Wang, Y. Tan, CO₂ hydrogenation to methanol over Cu/ZnO/ZrO₂ catalysts prepared by precipitation-reduction method, Appl. Catal. B Environ. 191 (2016) 8–17, <https://doi.org/10.1016/j.apcatb.2016.03.014>.
- [85] K. Larmier, W.C. Liao, S. Tada, E. Lam, R. Verel, A. Bansode, A. Urakawa, A. Comas-Vives, C. Copéret, CO₂-to-methanol hydrogenation on zirconia-supported copper nanoparticles: reaction intermediates and the role of the metal-support interface, Angew. Chem. Int. Ed. 56 (2017) 2318–2323, <https://doi.org/10.1002/anie.201610166>.
- [86] S. Kattel, B. Yan, Y. Yang, J.G. Chen, P. Liu, Optimizing binding energies of key intermediates for CO₂ hydrogenation to methanol over oxide-supported copper, J. Am. Chem. Soc. 138 (2016) 12440–12450, <https://doi.org/10.1021/jacs.6b05791>.
- [87] A. Le Valant, C. Comminges, C. Tisseraud, C. Canaff, L. Pinard, Y. Pouilloux, The Cu-ZnO synergy in methanol synthesis from CO₂, Part 1: Origin of active site explained by experimental studies and a sphere contact quantification model on Cu + ZnO mechanical mixtures, J. Catal. 324 (2015) 41–49, <https://doi.org/10.1016/j.jcat.2015.01.021>.
- [88] C. Peinado, D. Liuzzi, A. Sanchís, L. Pascual, M.A. Peña, J. Boon, S. Rojas, In situ conditioning of CO₂-rich syngas during the synthesis of methanol, Catalysts 11 (2021), <https://doi.org/10.3390/catal11050534>.
- [89] T. Lunkenbein, J. Schumann, M. Behrens, R. Schlögl, M.G. Willinger, Formation of a ZnO overlayer in industrial Cu/ZnO/Al₂O₃ catalysts induced by strong metal-support interactions, Angew. Chem. - Int. Ed. 54 (2015) 4544–4548, <https://doi.org/10.1002/anie.201411581>.
- [90] S. Zander, E.L. Kunkes, M.E. Schuster, J. Schumann, G. Weinberg, D. Teschner, N. Jacobsen, R. Schlögl, M. Behrens, The role of the oxide component in the development of copper composite catalysts for methanol synthesis, Angew. Chem. Int. Ed. 52 (2013) 6536–6540, <https://doi.org/10.1002/anie.201301419>.
- [91] V. Schott, H. Oberhofer, A. Birkner, M. Xu, Y. Wang, M. Muhler, K. Reuter, C. Wöll, Chemical activity of thin oxide layers: strong interactions with the support yield a new thin-film phase of zno, Angew. Chem. Int. Ed. 52 (2013) 11925–11929, <https://doi.org/10.1002/anie.201302315>.
- [92] J.A. Rodriguez, P. Liu, D.J. Stacchiola, S.D. Senanayake, M.G. White, J.G. Chen, Hydrogenation of CO₂ to methanol: importance of metal-oxide and metal-carbide interfaces in the activation of CO₂, ACS Catal. 5 (2015) 6696–6706, <https://doi.org/10.1021/acscatal.5b01755>.